


Stabilizing Remote Entanglement via Waveguide Dissipation

Parth S. Shah^{1,2,†}, Frank Yang^{1,2,†}, Chaitali Joshi^{1,2,†} and Mohammad Mirhosseini^{1,2,*}

¹Moore Laboratory of Engineering, California Institute of Technology, Pasadena, California 91125, USA

²Institute for Quantum Information and Matter, California Institute of Technology, Pasadena, California 91125, USA

 (Received 23 February 2024; revised 4 July 2024; accepted 9 August 2024; published 6 September 2024)

Distributing entanglement between remote sites is integral to quantum networks. Here, we demonstrate the autonomous stabilization of remote entanglement between a pair of noninteracting superconducting qubits connected by an open waveguide on a chip. In this setting, the interplay between a classical continuous drive—supplied through the waveguide—and dissipation into the waveguide stabilizes the qubit pair in a dark state, which, asymptotically, takes the form of a Bell state. We use field-quadrature measurements of the photons emitted to the waveguide to perform quantum state tomography on the stabilized states, where we find a concurrence of $0.504^{+0.007}_{-0.029}$ in the optimal setting with a stabilization time constant of 56 ± 4 ns. We examine the imperfections within our system and discuss avenues for enhancing fidelities and achieving scalability in future work. The decoherence-protected steady-state remote entanglement offered via dissipative stabilization may find applications in distributed quantum computing, sensing, and communication.

DOI: [10.1103/PRXQuantum.5.030346](https://doi.org/10.1103/PRXQuantum.5.030346)

I. INTRODUCTION

Entanglement between distant physical systems is a crucial resource for quantum information processing. Over long distances, entanglement can make communication secure against eavesdropping and resilient to loss [1–3]. On shorter length scales, entanglement between distant noninteracting modules can help realize nonlocal gates in a quantum computer [4–7]. Remote entanglement can be created by the deterministic exchange of photons between remote sites (see, e.g., Refs. [8,9]). Alternatively, measurements can be used to “herald” entanglement in a probabilistic fashion (see, e.g., Refs. [10,11]). Once created, entangled states have to be protected until they can be used, a task that can be achieved via storage in quantum memories [3]. Current research is pursuing efficient means of generation, distribution, and storage of remote entanglement.

An entirely different approach to entanglement generation is *stabilization* using quantum reservoir engineering.

This method employs dissipation into a shared reservoir, in combination with continuous drives, to establish entanglement between two or more parties. Intriguingly, an engineered dissipation can not only create entanglement but also protect it—indefinitely—from decoherence [12–22]. Beyond entanglement generation, dissipative processes have also been studied for a variety of other tasks as an alternative to unitary gate operations [13,23–25]. Despite the wide interest in this area, however, stabilizing *remote* entanglement has remained elusive, primarily due to the challenge of engineering shared dissipation for remote sites.

Spontaneous emission into a photonic bath can provide a shared dissipation channel for remote quantum emitters. Such a system can be realized within the paradigm of waveguide quantum electrodynamics (QED), where two or multiple qubits—acting as quantum emitters—are strongly coupled to a shared waveguide. In this setting, the interference of photons emitted by the qubits can give rise to the formation of collective states that are protected from dissipation by their internal symmetries [26–30]. Theoretical work has proposed a variety of methods for stabilizing these dark states [31–42]. However, experimental demonstrations of these proposals have remained out of reach, owing to the need for components such as unidirectional or time-modulated qubit-photon coupling and the injection of nonclassical states into the waveguide, which are challenging to implement.

*Contact author: mohmir@caltech.edu; <http://qubit.caltech.edu>

†These authors contributed equally to this work.

Published by the American Physical Society under the terms of the [Creative Commons Attribution 4.0 International license](https://creativecommons.org/licenses/by/4.0/). Further distribution of this work must maintain attribution to the author(s) and the published article’s title, journal citation, and DOI.

Here, we stabilize remote entanglement by exploiting the emission into a one-dimensional (1D) photonic bath. In our experiment, a pair of superconducting qubits, which are connected via an open microwave waveguide on a chip, serve as remote quantum nodes. In following a previous theoretical proposal [43], our approach offers simplicity by relying on classical drives and conventional bidirectional qubit-photon couplings. The dark state in our experiment is formed via the precise tuning of the qubit transition frequencies, which is done to match the interqubit physical distance to the wavelength of the emitted photons. Supplying a continuous drive through the waveguide, we stabilize the dark state, which takes the form of a Bell state under strong drives asymptotically. We conduct quantum state tomography to quantify the degree of entanglement in the steady state of the system. Repeating the experiment with different settings, we find a maximum concurrence of $0.504^{+0.007}_{-0.029}$ (95% confidence interval) with a stabilization time constant of 56 ± 4 ns in our system. We study the trade-off between the stabilization time and the entanglement quality in the steady state and compare it with a numerical model that considers the noise sources in our experiment. Finally, we discuss future improvements in the experimental parameters, showing the feasibility of achieving fidelities exceeding 90% with reasonable improvements in thermalization and qubit coherence. Our experiment elucidates the practical challenges of reservoir engineering with an open waveguide and marks an important step toward realizing a modular network architecture in which multinode remote entanglement is created and accessed on demand via an open radiation channel.

II. THEORETICAL CONCEPT

Our system includes two qubits coupled to a shared waveguide with equal dissipation rates of Γ_{1D} [see Fig. 1(a)]. The qubit frequencies are offset symmetrically with respect to a center frequency ($\omega_{1,2} = \omega \pm \delta$). Further, we choose the center frequency ω such that $\ell = m\lambda$, where ℓ is the physical distance between the qubits, λ is the wavelength of radiation at ω , and m is an integer. We assume that the qubits are driven via a classical coherent field at the frequency ω , supplied through the waveguide. In a frame rotating at the driving frequency, and after applying the rotating-wave approximation (RWA), the Hamiltonian for this system can be written as

$$\hat{H}/\hbar = \sum_{i=1,2} \frac{\delta_i}{2} \hat{\sigma}_{z,i} + \frac{1}{2} \left(\Omega \hat{\sigma}_i^\dagger + \Omega^* \hat{\sigma}_i \right). \quad (1)$$

Here, Ω denotes the Rabi frequency of the drive and $\delta_{1,2} = \pm\delta$. While this Hamiltonian is separable, the interference of photons emitted by the two qubits in this setting gives rise to suppression and enhancement of spontaneous emission [44]. These effects can be taken into account by rewriting the Hamiltonian in the basis of triplet and singlet states $|T, S\rangle = (|eg\rangle \pm |ge\rangle)/\sqrt{2}$, finding

$$\hat{H}/\hbar = \frac{\Omega}{\sqrt{2}} (|T\rangle\langle gg| + |ee\rangle\langle T|) - \delta (|S\rangle\langle T|) + \text{H.c.} \quad (2)$$

In Fig. 1(b) (left), we show the corresponding energy-level diagram, including the coupling and dissipation terms (for the derivation, see Appendix B 1). As is evident, the singlet state is subradiant and is protected from

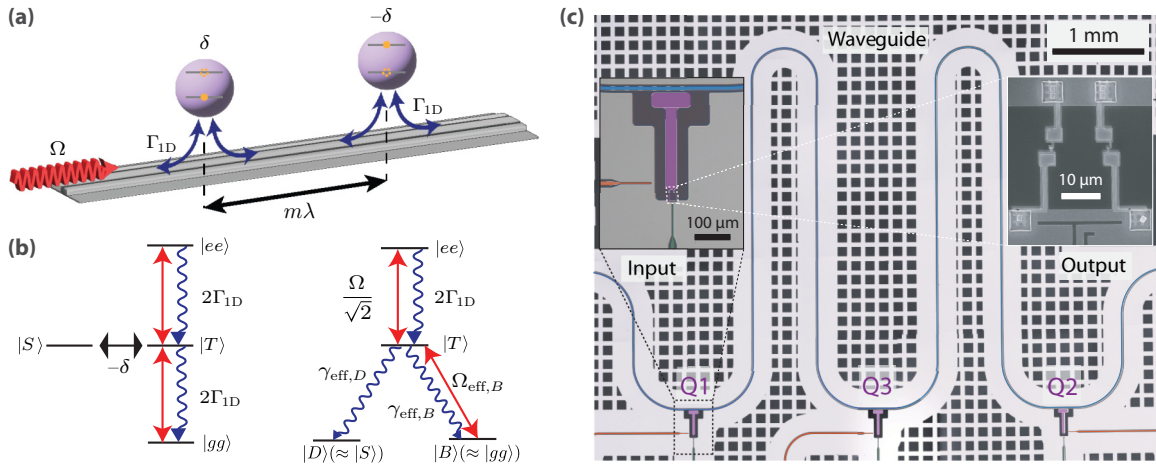


FIG. 1. The experimental setup. (a) A pair of quantum emitters coupled to a shared waveguide. The qubit transition frequencies are offset in opposite directions with respect to a central frequency and their separation is set equal to the wavelength at this center frequency. A continuous Rabi drive is supplied through the channel. (b) Left: the energy-level diagram of the system. The triplet state $|T\rangle$ superradiantly decays into the waveguide. The singlet state $|S\rangle$ is coherently coupled to the triplet but has no direct decay path into the waveguide. Right: the energy diagram in a basis including the dark state $|D\rangle$. Here, the population is pumped from the triplet into the dark state, which is protected from decay into the waveguide. (c) An optical image of the fabricated device, where three transmon qubits are coupled to a shared coplanar waveguide on a chip.

direct dissipation into the waveguide. However, the singlet state exchanges population with the waveguide indirectly through coherent interaction with the triplet state, which is superradiant. In the steady state, the combination of this interaction and continuous drive through the waveguide creates a superposition of the singlet and the ground states that is completely dark to the waveguide. This stationary dark state is given by (see Appendix B 2 and [35,43])

$$|D\rangle = \frac{|gg\rangle + \alpha|S\rangle}{\sqrt{1 + |\alpha|^2}}. \quad (3)$$

Here, $\alpha = \Omega/\sqrt{2}\delta$ is a drive-power-dependent parameter that sets the singlet fraction ($|\alpha|^2/(1 + |\alpha|^2)$). As is evident, the stationary state is pure and for strong drives ($|\alpha| \gg 1$) approaches the maximally entangled singlet state. As a result, by simply supplying the drive into the waveguide, one can stabilize entanglement between the qubits starting from an arbitrary initial state.

By redrawing the energy-level diagram to include the dark state, $|D\rangle$, and a state orthogonal to it in the $\{|gg\rangle, |S\rangle\}$ subspace, $|B\rangle = (\alpha|gg\rangle - |S\rangle)/\sqrt{1 + |\alpha|^2}$, one can find the rate of pumping population into $|D\rangle$. As shown in Fig. 1(b) (right), the population is dissipatively transferred from $|T\rangle$ to $|D\rangle$, where it is trapped due to the decoupling of the dark state from the remainder of the energy levels. The effective rate of this process can be found as (for the derivation, see Appendix B 2)

$$\gamma_{\text{eff},D} = \frac{2\Gamma_{1D}}{1 + \Omega^2/2\delta^2}. \quad (4)$$

The reciprocal of this ‘‘pumping’’ rate $t_D = 1/\gamma_{\text{eff},D}$ sets the approximate time scale for stabilization of the dark state and therefore sets the rate of entanglement generation. We highlight the competition between the singlet fraction $|\alpha|^2/(1 + |\alpha|^2)$ and the relaxation time $t_D = (1 + |\alpha|^2)/(2\Gamma_{1D})$, where achieving larger singlet fractions—corresponding to more entanglement—requires higher drive powers and longer relaxation times. This trade-off is illustrated by the $\delta = 0$ case, which corresponds to stabilizing a pure Bell state $|D\rangle = |S\rangle$ but takes infinitely long to stabilize $\gamma_{\text{eff},D} \rightarrow 0$ (for further discussion, see Appendixes B 2 and G 2).

To successfully implement the stabilization protocol under consideration, a physical platform must fulfill several requirements. Most importantly, it is necessary to have precise control over the qubit transition frequency and to establish efficient interfaces between qubit and propagating photons. Precise control over the qubit frequency is needed to ensure that the interference of emitted photons leads to destructive interference at both the outputs of the waveguide simultaneously, culminating in a dark state. Formally, this condition can be articulated by defining the null spaces for the collective jump operators (see

Appendix B 2) [45]. As shown in Ref. [43], deviations of the drive frequency from the center frequency ω result in the dark state having an additional loss mechanism, thereby limiting the achievable entanglement. Efficient qubit-photon interfaces are vital to minimize photon loss during the emission and reabsorption processes among the qubits, which can result in a reduced fidelity for the stabilized state. A key metric in evaluating this effect is the Purcell factor, defined as the ratio of the decay rate of an individual qubit to the waveguide to its intrinsic decoherence rate, $P_{1D} = \Gamma_{1D}/\Gamma'$, where $\Gamma' = 2\Gamma_2 - \Gamma_{1D} = \Gamma_{\text{int}} + 2\Gamma_\phi$. (Γ_2 is the total qubit decoherence, Γ_{int} is the loss to nonradiative channels, and Γ_ϕ is the pure dephasing.) In addition to the factors mentioned, another key ingredient is the characterization of the stabilized joint qubit state. This task is particularly challenging in the presence of dissipation from the waveguide. To overcome this challenge, characterization measurements need to happen either on very short time scales or, alternatively, temporary elimination of waveguide dissipation is needed during the characterization process. In Sec. III, we detail an experimental realization based on transmon superconducting qubits that satisfies these requirements.

III. EXPERIMENT

The fabricated superconducting circuit used to realize our experiment is shown in Fig. 1(c). The circuit consists of three transmon qubits (1, 2, and 3), which are side coupled to the same coplanar waveguide (CPW). Each qubit has a weakly coupled charge control line (shown in orange) and an external flux bias port (shown in green) for tuning its transition frequency. Qubit 3 does not participate in any of our experiments and is decoupled from the rest of the system by tuning its frequency well away (>1 GHz) from the other two qubits. The device fabrication is described in Appendix A.

We first verify the required interference conditions by looking for signatures of the subradiant and superradiant states. In Fig. 2(a), we show the transmission through the waveguide for weak microwave drives, measured as a function of the flux bias of qubit 1. Meanwhile, qubit 2 has its transition frequency fixed at ω such that the interqubit separation along the waveguide equates to the corresponding wavelength ($\ell = \lambda$). As the two qubits cross, we note a broader resonant line shape, indicating the formation of a superradiant state [44]. In Fig. 2(b), we show the waveguide transmission for two qubits that are precisely on resonance at ω (red) and for qubit 2 at ω while qubit 1 is tuned out of the measurement window (blue). By fitting Lorentzian line shapes to these spectra, we find the radiative decay rate of the superradiant (triplet) state, $\Gamma_{1D,T}/2\pi = 18.3$ MHz, which is nearly twice the single-qubit decay rate $[(\Gamma_{1D,1}, \Gamma_{1D,2})/2\pi = (10.3, 10.7)$ MHz], pointing to the correct phase length between the

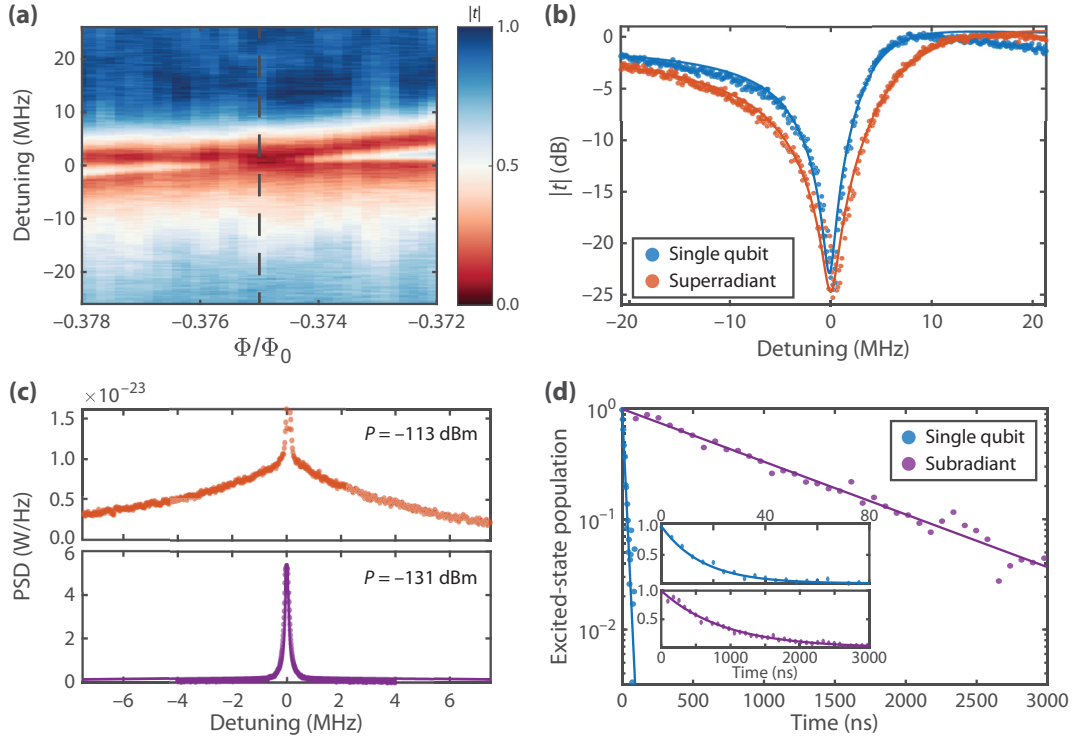


FIG. 2. Characterizing the super- and subradiant collective states. (a) The transmission spectrum measured through the waveguide as qubit 1 is frequency-tuned across qubit 2. The dashed line denotes the $\ell \approx \lambda$ point. (b) The transmission spectra for the single qubit (qubit 2, blue) and two-qubit (red) settings, where a broader spectrum indicates the superradiant (triplet) state. (c) The inelastic scattering spectrum. At higher drive powers (upper inset), the line shape includes contributions from both the triplet and singlet states. Reducing the drive power results in a line shape predominantly set by the singlet state, which is fitted to a master-equation simulation. (d) The measured relaxation lifetimes for an individual qubit (qubit 2) and the singlet state, yielding $T_1 = 16 \pm 1.9$ ns and $T_1 = 910 \pm 47$ ns, respectively. The insets show the linear-scale plots of the same data.

qubits. We extract individual-qubit Purcell factors (at ω) of $[(P_{1D,1}, P_{1D,2}) = (11.4, 10.7)]$.

Although the singlet is (ideally) protected from emission to the waveguide, emission can be caused by dephasing or imbalanced waveguide decay rates between qubits, which prevent ideal destructive interference. The elastic scattering in this case is dominated by the bright-state response and does not provide a good measure of emission from the singlet. To probe the singlet, we instead measure the inelastic scattering from the qubits using a spectrum analyzer (see Appendix A). While the resonance fluorescence spectrum at higher powers contains contributions from both the super- and subradiant states, a measurement done at a sufficiently low drive power is dominated by the response from the subradiant (singlet) state, as shown in Fig. 2(c) [26]. A master-equation simulation fit to the inelastic scattering profile confirms the presence of the subradiant state (for a detailed discussion, see Appendix C). Furthermore, we measure the population decay lifetimes of the singlet and an individual qubit (described in Appendix D [28]), shown in Fig. 2(d). We find a large contrast (a factor of over 50) in the measured lifetimes, indicating that the qubit-frequency

configuration and the Purcell factors are suitable for the realization of the stabilization protocol.

Having established the operation frequency, we proceed with the stabilization and characterization of entangled states. In this step, the qubits are detuned with respect to the target frequency [see Fig. 3(a) and Appendix G2]. Starting with a system at rest in $|gg\rangle$, we apply a narrow-band drive at ω to initiate the stabilization process. While the drive is being supplied, the population is coherently driven from $|gg\rangle$ to $|T\rangle$, where it decays to the dark state $|D\rangle$ ($|B\rangle$) with rate $\gamma_{\text{eff},D}$ ($\gamma_{\text{eff},B}$). The population in $|B\rangle$ is then continuously driven to $|T\rangle$, while $|D\rangle$ decouples from the dynamics. After supplying the drive for a finite duration of time, we turn it off and allow the qubits to decay freely into the waveguide. We note here that the short radiative lifetime of the qubits (caused by waveguide dissipation) precludes the use of dispersive readout. As an alternative, we characterize the state of the qubits using the photons emitted into the waveguide. The photons originating from each qubit in our experiment are spectrally distinguishable because of the large detuning between the qubits. Using quadrature amplitude detection and mode

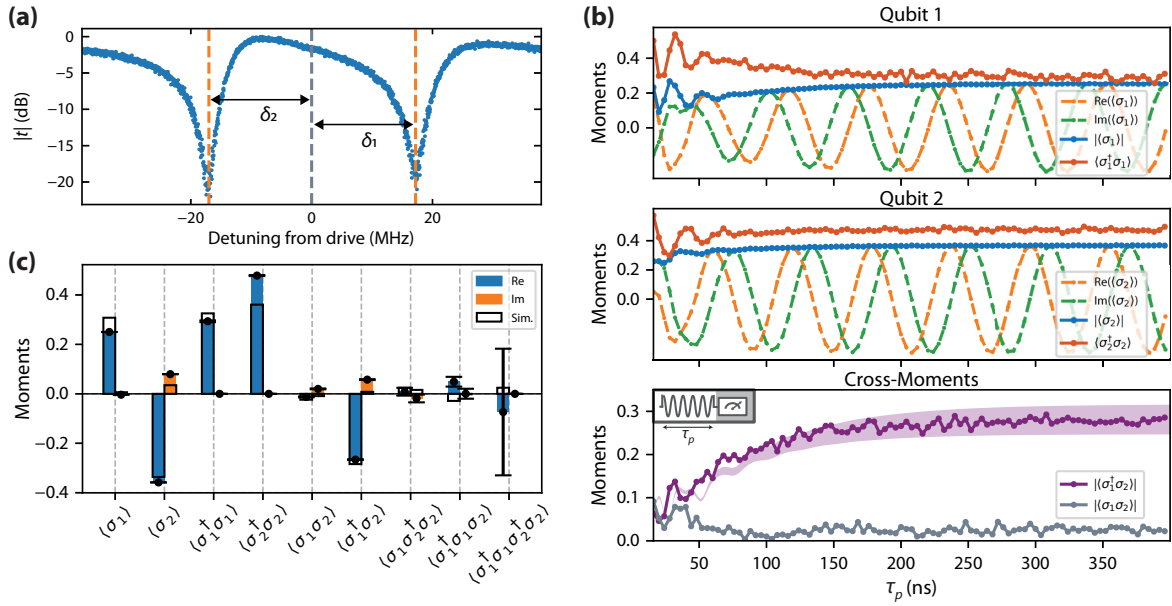


FIG. 3. The stabilization dynamics. (a) The transmission spectrum measured through the waveguide when the two qubits are detuned symmetrically ($\delta_1/2\pi = -\delta_2/2\pi = \delta/2\pi = 17$ MHz). The gray dashed line marks the target drive frequency ($\omega/2\pi = 6.392$ GHz, where $\ell \approx \lambda$). (b) The time dynamics of the first- and second-order moments after supplying a continuous drive with a power of -117 dBm (corresponding to $\Omega_1/2\pi = 36$ MHz and $\Omega_2/2\pi = 37$ MHz) and a frequency of ω to the waveguide. The inset shows the pulse scheme, where we apply a constant pulse for τ_p ns and then immediately measure the state of the qubits. The plots display average values derived from an experiment that has been repeated 150×10^6 times, with a delay between each measurement (200 ns, much longer than the radiative lifetime of the individual qubits) ensuring that the system is at “rest” prior to the subsequent measurement. Note that the time axis starts from a drive length of 16 ns. (c) The measured moments of the stabilized state, after a long drive (396 ns). The plot includes all nonzero terms for an arbitrary state residing in a Hilbert space containing at most a single excitation in each qubit. The plots display average values derived from an experiment that has been repeated 3×10^9 times and the horizontal bars indicate standard deviations (see Appendix E 4). The values from a numerical simulation with experimental parameters are displayed for comparison (boxed outlines). For further simulation details, see Appendix G.

matching to the photonic time bins (following previous work, [46–49]) we successfully measure the self- and cross-moments of the emitted photons. Through input-output relations of multiple qubits coupled to an open waveguide, we can relate these photonic moments to those of the qubits themselves. Additionally, since each photon is emitted by a qubit, it may at most have only one excitation. Therefore, computing all the self- and cross-moments of the form $\langle (\hat{\sigma}_1^\dagger)^{n_1} \hat{\sigma}_1^{m_1} (\hat{\sigma}_2^\dagger)^{n_2} \hat{\sigma}_2^{m_2} \rangle \forall n_1, n_2, m_1, m_2 \in \{0, 1\}$ suffices to perform a joint state tomography of the two-qubit state (see Appendix E).

In Fig. 3(b), we show the measured self- and cross-moments of the qubits as the state evolves in time for a Rabi drive of $\Omega/2\pi = 37$ MHz and a detuning of $\delta/2\pi = 17$ MHz between the qubits and the drive. With the continuous drive turned on, we observe an initial increase in the average population of each qubit with time, followed by settling into a steady-state value. The stabilization of an entangled dark state can be identified via the emergence and stabilization of a nonzero cross-qubit moment $\langle \hat{\sigma}_1^\dagger \hat{\sigma}_2 \rangle$. We also note the nonzero expectation values of the single-qubit first moments $\langle \hat{\sigma}_i \rangle$, which can be attributed

to the finite population of the ground state that still has coherence with the excited-state populations. In Fig. 3(c), we show the measurement results of the steady state and include all relevant moments for any joint two-qubit state. The small magnitudes of the third and fourth moments indicate the low population of the doubly excited state $|ee\rangle$. Using the computed moments, we reconstruct the density matrix for the two-qubit system using maximum-likelihood estimation (Appendix E 4). The fidelity of the extracted density matrix to the singlet state at this drive power and detuning is $56.5_{-1.3}^{+2.2}\%$ (95% confidence interval), which is already above the 50% threshold that confirms entanglement.

Beyond the quality of entanglement, the stabilization rate (γ_{eff}) is another important metric for practical applications. In the protocol being examined, the stabilization rate is anticipated to decrease as the drive power increases, as indicated by Eq. (4). At the same time, the level of entanglement, quantified by the singlet fraction [see Eq. (3)], is expected to rise with increasing drive power. In Fig. 4(a), we show the time evolution of the cross-moment $\langle \hat{\sigma}_1^\dagger \hat{\sigma}_2 \rangle$ across three different power levels. The stabilization rates,

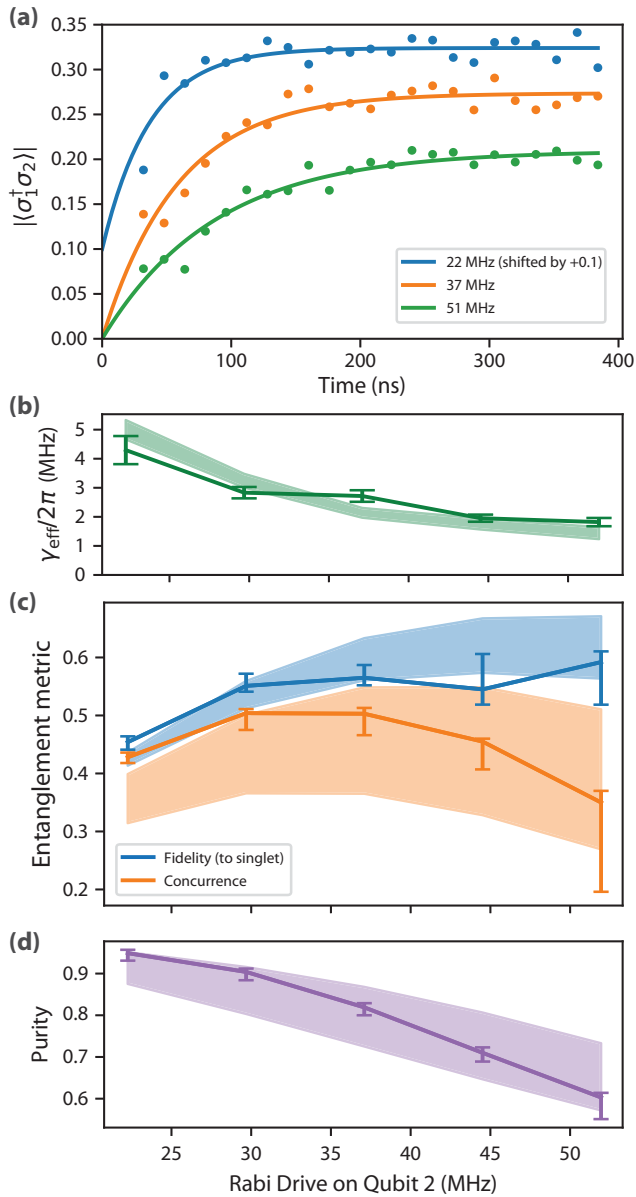


FIG. 4. The interplay between the drive power, the stabilization rate, and entanglement. (a) The stabilization dynamics for different drive powers, showing the $\langle \hat{\sigma}_1^\dagger \hat{\sigma}_2 \rangle$ cross-moment. Exponential fits (solid lines) to measured data (dots) give us the stabilization rates, γ_{eff} , for different drive powers. (b) Variation in the stabilization rates with the power. The error bars represent \pm standard deviations. (c) The fidelity (to a singlet state) and concurrence versus the drive power. The error bars represent the 95% confidence interval. (d) The purity as a function of the drive power. The error bars represent the 95% confidence interval. The shaded regions in (b)–(d) represent simulation results with varying Purcell factors (from 10 to 30) for the qubits (see Appendix G).

derived from exponential fits to the cross-moments versus time, exhibit a consistent decline with increased power, aligning with our expectations [see Fig. 4(b)]. Note that γ_{eff} here does not strictly correspond to $\gamma_{\text{eff},D}$ given in Eq. (4),

which defines the decay rate from $|T\rangle$ to $|D\rangle$. We also plot the fidelity relative to the singlet state for each power setting [see Fig. 4(c)], revealing that the fidelities initially rise with the power before saturating.

To more accurately assess entanglement, we calculate the concurrence [50] for each power setting [see Fig. 4(c)]. The concurrence peaks at intermediate drive powers and reduces at both lower and higher powers. The reduction of entanglement at low powers aligns with expectations, mirroring the calculated fidelity and analytical predictions. Reduced entanglement at high power can be qualitatively understood by considering the role of parasitic (i.e., non-radiative) damping and dephasing, which our analytical model does not capture. Intuitively, these effects drive the qubits toward a mixed state, with the decoherence rate Γ' competing against the dark-state pumping rate $\gamma_{\text{eff},D}$ [34]. This explanation is supported by the calculated purity of the stabilized states, which drop from $90.4^{+0.8}\%$ at $\Omega/2\pi = 30$ MHz to $60.3^{+1.1}\%$ at $\Omega/2\pi = 51$ MHz [Fig. 4(d)]. We use master-equation simulations to account for parasitic damping and dephasing in our experiment. A complicating factor here is power-dependent dephasing in driven qubits [51,52], which results in a variable Purcell factor at different drive powers (see Appendix F). To capture this phenomenon, we conduct simulations for a range of Purcell factors, setting the lower limit based on our qubit transmission measurements ($P_{1D} = 10$) and selecting an upper bound that qualitatively aligns with our experimental data ($P_{1D} = 30$). The simulations, depicted in Figs. 4(b)–4(d), qualitatively mirror the observed power-dependent variations in our experimental results. In our system, we achieve a maximum concurrence of $0.504^{+0.007}_{-0.029}$ at an optimal drive power of $\Omega/2\pi = 30$ MHz. The corresponding time constant is 56 ± 4 ns, giving a stabilization rate of $2.83 (\pm 0.19)$ MHz, which is comparable to previous demonstrations with superconducting qubits [9,53–55].

IV. CONCLUSIONS AND OUTLOOK

Remote entanglement is a crucial resource for quantum networks, with a wide range of applications in distributed quantum computing, communication, and sensing. In platforms equipped with low-loss communication channels, such as superconducting qubits, remote entanglement has been produced through deterministic processes involving direct photon exchange [8,54,56,57] or virtual interactions via cavity relays [9,55,58,59]. Although these methods have achieved high fidelities, they typically require pulse shaping or precise timing of qubit operations. Relying on driven-dissipative stabilization, as showcased in our experiment, offers a simple alternative that relaxes these requirements. Additionally, stabilizing the target state allows for maintaining the entanglement indefinitely, until it is

needed for quantum networking operations, thereby providing an on-demand resource without the latency caused by the propagation delay between the nodes.

In terms of physical dimensions, the interqubit distance in our experiment is not particularly long (all components are confined within a 1-cm \times 1-cm chip) and is comparable to previous work in cavity systems [18,20–22]. Distinctly, however, relying on an open waveguide makes the concept insensitive to the distance between the qubits (within integer multiples of $\lambda/2$), allowing for the stabilization of long-distance entanglement. This increased range of entanglement is not limitless, as the breakdown of the Markov approximation (inherently assumed in our analysis) sets an upper bound on the distance. Nonetheless, with the dissipation and drive rates attainable with superconducting qubits, this limit is rather long (meters), allowing for the method to be practically feasible for a range of applications. Going beyond this limit remains relatively unexplored, though proposals based on injecting squeezed light into waveguides may provide a route toward this [39,41]. Additionally, the broadband nature of the waveguide enables frequency multiplexing, permitting the simultaneous entanglement of multiple qubit pairs at different frequencies through the same channel. Finally, the use of chiral qubit-photon coupling [60–65] can relax the requirement of precise phase tuning between the qubits and also lead to the formation of multipartite entanglement [35,43].

In terms of entanglement fidelity, we achieve only modest results, which are limited by the qubit coherence (see Appendix H) and noise introduced by the broadband waveguide bath. While previous demonstrations have used lossy cavities as engineered reservoirs, a genuine continuum of photonic states (i.e., a waveguide) is needed to stabilize long-distance remote entanglement. However, the nominally infinite bandwidth of a waveguide provides additional challenges as compared to a cavity; noise sources arising from a finite temperature or from classical sources [66] contribute to reduced fidelities. Propagation losses in the waveguide add additional complexity [67] and may potentially prevent the required interference. In our protocol, with improvements to the qubit coherence and waveguide temperature, we expect fidelities of over 90% (concurrence of 0.88) to be within reach, with concomitantly reduced stabilization rates of 250 kHz. Ultimately, going beyond these limits requires further investigations of protocols with better hardware efficiency and improved bandwidths [68].

In conclusion, we have demonstrated the generation and stabilization of entanglement between a pair of distant qubits coupled to a shared waveguide via a driven-dissipative protocol. The presented scheme offers simplicity, steady-state operation, and decoherence protection, making it an attractive avenue for remote-entanglement generation. We have also identified the

limitations of our experiment, finding high-fidelity remote entanglement to be achievable using qubits with improved decoherence characteristics well within reach of existing superconducting technologies. With future improvements in fidelities, we envision that entanglement-stabilization protocols may find applications in distributed quantum computing and quantum communication.

ACKNOWLEDGMENTS

This work was supported by start-up funds from Caltech’s Engineering and Applied Science (EAS) division, the National Science Foundation (NSF) (Award No. 1733907), and the Office of Naval Research (Award No. N00014-24-1-2052). P.S.S. gratefully acknowledges support from the S2I-Gupta Fellowship. F.Y. gratefully acknowledges support from the NSF Graduate Research Fellowship. C.J. gratefully acknowledges support from the Institute for Quantum Information and Matter (IQIM)—Amazon Web Services (AWS) Postdoctoral Fellowship.

APPENDIX A: METHODS

1. Fabrication

Our device is fabricated on a 1-cm \times 1-cm high-resistivity (10-k Ω -cm) silicon substrate. Electron-beam lithography is used to pattern the structures in separate metal layers on the chip. Each lithography step is followed by electron-beam evaporation of metal and lift-off in *N*-methyl-2-pyrrolidone at 150 $^{\circ}$ C for 1.5 h. The device layers are as follows:

- (i) 150-nm-thick niobium markers, deposited at 3 $\text{\AA}/\text{s}$.
- (ii) 120-nm-thick aluminum ground plane, waveguide, flux lines, and qubit capacitors, deposited at 5 $\text{\AA}/\text{s}$.
- (iii) Josephson junctions evaporated (at 5 $\text{\AA}/\text{s}$) using double-angle evaporation and consisting of 60- and 120-nm layers of aluminum, with 15-min static oxidation between layers. We use asymmetric Josephson junctions in the superconducting quantum interference device (SQUID) loop of each qubit to mitigate the effects of dephasing [69] (for further details, see the device parameters given in Table I).
- (iv) 150-nm-thick aluminum band-aids and air bridges, deposited at 5 $\text{\AA}/\text{s}$. The band-aids ensure electrical contact between Josephson junctions and qubit capacitors. The air bridges are used to ensure the suppression of the slot-line modes in the waveguide [70]. The air bridges are patterned using grayscale electron-beam lithography and developed in a mixture of isopropyl alcohol and deionized water, followed by 10 min of reflow at 105 $^{\circ}$ C [71]. Electron-beam evaporation of the band-aid/air-bridge layer is preceded by 7 min of Ar ion milling.

TABLE I. A summary of the experimental parameters.

Description	Symbol	Value
<i>Qubit 1</i>		
Minimum frequency	$\omega_{1, \min}/2\pi$	6.409 GHz
Maximum frequency	$\omega_{1, \max}/2\pi$	7.505 GHz
Total Josephson energy	$E_J (= E_{J,a} + E_{J,b})$	25.4 GHz
Junction asymmetry	$\alpha_J (= E_{J,a}/E_{J,b})$	6.6
Anharmonicity	$E_c (= -\alpha)$	311 MHz
<i>Qubit 2</i>		
Minimum frequency	$\omega_{2, \min}/2\pi$	6.343 GHz
Maximum frequency	$\omega_{2, \max}/2\pi$	7.457 GHz
Total Josephson energy	$E_J (= E_{J,a} + E_{J,b})$	25.1 GHz
Junction asymmetry	$\alpha_J (= E_{J,a}/E_{J,b})$	6.5
Anharmonicity	$E_c (= -\alpha)$	315 MHz
<i>Qubit 3</i>		
Minimum frequency	$\omega_{3, \min}/2\pi$	6.565 GHz
Maximum frequency	$\omega_{3, \max}/2\pi$	7.640 GHz
Total Josephson energy	$E_J (= E_{J,a} + E_{J,b})$	26.3 GHz
Junction asymmetry	$\alpha_J (= E_{J,a}/E_{J,b})$	6.9
Anharmonicity	$E_c (= -\alpha)$...
<i>Super- (sub-) radiant state (Fig. 2)</i>		
Waveguide distance	$\ell (= \lambda)$	18.2 mm
Qubit-1 waveguide decay	$\Gamma_{1D,1}/2\pi$	10.3 ± 0.3 MHz
Qubit-1 intrinsic decoherence	$\Gamma'_1/2\pi$	0.9 ± 0.4 MHz
Qubit-1 Purcell factor	$P_{1D,1} (= \Gamma_{1D,1}/\Gamma'_1)$	11.4
Qubit-2 waveguide decay	$\Gamma_{1D,2}/2\pi$	10.7 ± 0.4 MHz
Qubit-2 intrinsic decoherence	$\Gamma'_2/2\pi$	1.0 ± 0.5 MHz
Qubit-2 Purcell factor	$P_{1D,2} (= \Gamma_{1D,2}/\Gamma'_2)$	10.7
Superradiant-state waveguide decay	$\Gamma_{1D,T}/2\pi$	18.3 ± 0.4 MHz
Superradiant-state intrinsic decoherence	$\Gamma'_T/2\pi$	1.3 ± 0.5 MHz
Qubit-1 lifetime	$T_{1,1}$	16.6 ± 0.6 ns
Qubit-2 lifetime	$T_{1,2}$	16.0 ± 1.9 ns
Subradiant-state lifetime	$T_{1,S}$	910 ± 47 ns
<i>Stabilization experiment (Fig. 3)</i>		
Drive frequency	$\omega/2\pi$	6.392 GHz
Qubit-1 waveguide decay	$\Gamma_{1D,1}/2\pi$	8.7 ± 0.1 MHz
Qubit-1 intrinsic decoherence	$\Gamma'_1/2\pi$	1.5 ± 0.2 MHz
Qubit-1 Purcell factor	$P_{1D,1} (= \Gamma_{1D,1}/\Gamma'_1)$	5.8
Qubit-2 waveguide decay	$\Gamma_{1D,2}/2\pi$	10.5 ± 0.1 MHz
Qubit-2 intrinsic decoherence	$\Gamma'_2/2\pi$	1.3 ± 0.2 MHz
Qubit-2 Purcell factor	$P_{1D,2} (= \Gamma_{1D,2}/\Gamma'_2)$	8.1

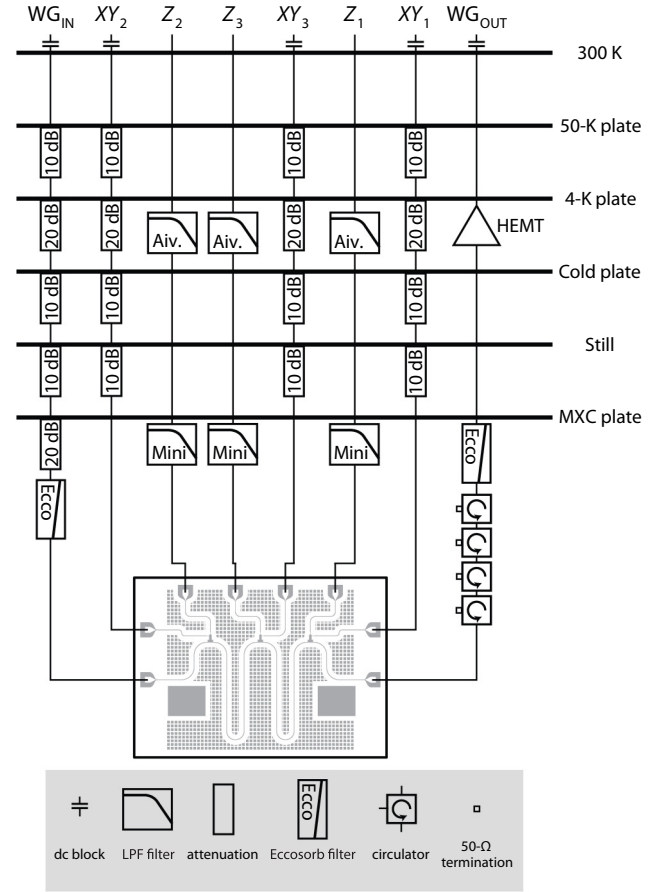


FIG. 5. The measurement setup. A schematic of the dilution fridge wiring for measurement.

2. Measurement setup

The measurements are performed in a ^3He - ^4He dilution refrigerator. A schematic of our measurement setup is shown in Fig. 5. The fabricated chip is wire bonded to a printed circuit board (PCB) and placed in a copper box. The box is then mounted to the mixing plate, which is cooled to a base temperature of 10 mK.

The waveguide input line (“WG_{IN}”) is used to drive the qubits and is attenuated at each temperature stage to minimize thermal noise; the total attenuation is 70 dB. Attenuators (not shown) are added to the input line at room temperature to control the input power. Four isolators are used to reduce thermal noise in the waveguide output line (“WG_{OUT}”). The output is amplified by a high-electron-mobility transistor (HEMT) amplifier at the 4-K stage and a room-temperature amplifier (not shown) outside of the fridge.

A low-noise multichannel dc source provides current biases to flux tune the qubit frequencies. Low-pass rf filters (Aivon Therna-uD25-GL RC filter with 15-kHz cutoff frequency, Mini-Circuits VLFG490+ with 490-MHz cutoff frequency) suppress high-frequency thermal noise in

the dc lines, which are not attenuated. The qubits are also equipped with XY drive lines and the rf inputs to the drive lines are attenuated (50-dB total) to reduce thermal noise.

a. Spectral measurements

The elastic scattering measurements [Figs. 2(a), 2(b), and 3(a)] are performed using a vector network analyzer (VNA, Agilent N5242A). The VNA drives are attenuated to sub-single-photon power levels in order to prevent qubit saturation. The nonlinear least-squares method or circle-fit method is used to fit the transmission traces. The inelastic scattering measurements [Fig. 2(c)] are performed with an rf spectrum analyzer (Rohde & Schwarz FSV3013); the VNA in zero-span mode provides the microwave excitation tone. The spectrum-analyzer acquisition is performed with a resolution bandwidth of 20 kHz. The measured resonance fluorescence of the subradiant state is fitted to master-equation simulations, as discussed in Appendix C.

b. State tomography

Qubit state tomography is performed using the Quantum Machines OPX+ (QM) module, which is capable of arbitrary waveform generation and heterodyne detection. To generate the drive, megahertz-frequency intermediate frequency (IF) signals from the QM are combined with a local oscillator (LO) supplied by an rf signal generator (Rohde & Schwarz SMB100) using in-phase and quadrature (IQ) mixers (Marki Microwave MMIQ-0520LS). For readout, the signal from the output line is down-converted using an IQ mixer and the resulting IF signal is digitally demodulated. Details of the state tomography are discussed in Appendix E 1. The data presented in Fig. 2(d); Figs. 3(b) and 3(c); and Figs. 4(a) and 4(b) are recorded using state tomography techniques.

3. Device parameters

The relevant device parameters are given in Table I.

APPENDIX B: THEORETICAL MODELING

Here, we present the theoretical framework used to model two driven qubits coupled to a waveguide and the stabilization of the entangled dark state.

1. Master equation

The most general master equation for this system is given by [43,44,72].

$$\dot{\rho} = -\frac{i}{\hbar}[\hat{H} + \hat{H}_{\text{int}}, \rho] + \mathcal{L}\rho, \quad (\text{B1})$$

where

$$\hat{H}/\hbar = \sum_{i=1,2} \frac{\delta_i}{2} \hat{\sigma}_{z,i} + \frac{1}{2} \left(\Omega_i \hat{\sigma}_i^\dagger + \Omega_i^* \hat{\sigma}_i \right) \quad (\text{B2})$$

is the system Hamiltonian written in the drive frame after applying the RWA. Both qubits are driven at the same frequency ω , such that $\delta_i = \omega_i - \omega$ is the qubit-drive detuning (ω_i is the frequency of qubit i). Ω_i denotes the Rabi frequency on each qubit. In the case of a drive applied via the waveguide (corresponding to our experiment), $\Omega_i = |\Omega_i| e^{ikx_i}$ includes the propagation phase accumulated by the drive. Here, x_i is the position of qubit i and $k = n\omega/c$ is the wave vector of the drive (n denotes the refractive index and c denotes the speed of light). \hat{H}_{int} denotes the photon-mediated interaction:

$$\hat{H}_{\text{int}}/\hbar = J \hat{\sigma}_1^\dagger \hat{\sigma}_2 + J^* \hat{\sigma}_2^\dagger \hat{\sigma}_1. \quad (\text{B3})$$

Here, $J = \sqrt{\Gamma_{1D,1}\Gamma_{1D,2}}(e^{+ik_2d} - e^{-ik_1d})/4i$. For the case of two qubits at the same frequency, this expression simplifies to the more familiar $J = (\sqrt{\Gamma_{1D,1}\Gamma_{1D,2}}/2) \sin(kd)$ [44]. Here, $\Gamma_{1D,i}$ is the dissipation rate of qubit i into the waveguide, k_i is the wave vector at ω_i , and $d = |x_2 - x_1|$ is the qubit separation. The Liouvillian is given by

$$\mathcal{L}\rho = \Gamma_{1D,1}\mathcal{D}[\hat{\sigma}_1]\rho + \Gamma_{1D,2}\mathcal{D}[\hat{\sigma}_2]\rho + \Gamma_{12}\mathcal{D}[\hat{\sigma}_1, \hat{\sigma}_2]\rho + \Gamma_{21}\mathcal{D}[\hat{\sigma}_2, \hat{\sigma}_1]\rho. \quad (\text{B4})$$

Here, $\Gamma_{12} = \Gamma_{21}^* = \sqrt{\Gamma_{1D,1}\Gamma_{1D,2}}(e^{+ik_2d} + e^{-ik_1d})/2$, which simplifies to $\Gamma_{12} = \sqrt{\Gamma_{1D,1}\Gamma_{1D,2}} \cos(kd)$ for resonant qubits. This term denotes the correlated decay between qubits. The dissipator terms in the above equation are given by

$$\mathcal{D}[A]\rho = A\rho A^\dagger - \frac{1}{2}A^\dagger A\rho - \frac{1}{2}\rho A^\dagger A, \quad (\text{B5})$$

$$\mathcal{D}[A, B]\rho = B\rho A^\dagger - \frac{1}{2}A^\dagger B\rho - \frac{1}{2}\rho A^\dagger B. \quad (\text{B6})$$

In our experiment, we drive both qubits through the waveguide at a frequency ω corresponding to qubit separation of λ . We then have $\Omega_1 = \Omega_2$. Additionally, each qubit is equally detuned from the drive frequency so that $\omega_{1,2} = \omega \pm \delta$. At this detuning setting, the photon-mediated interaction (J) disappears exactly and the Hamiltonian is fully described by Eq. (1), reproduced as

$$\hat{H}/\hbar = \sum_{i=1,2} \frac{\delta_i}{2} \hat{\sigma}_{z,i} + \frac{1}{2} \left(\Omega \hat{\sigma}_i^\dagger + \Omega^* \hat{\sigma}_i \right). \quad (\text{B7})$$

Using the triplet and singlet states $|T, S\rangle = (|eg\rangle \pm |ge\rangle)/\sqrt{2}$, we can then rewrite the Hamiltonian as in

Eq. (2), repeated as

$$\hat{H}/\hbar = \frac{\Omega}{\sqrt{2}} (|T\rangle\langle gg| + |ee\rangle\langle T|) - \delta (|S\rangle\langle T|) + \text{H.c.} \quad (\text{B8})$$

For this detuning setting, the correlated decay becomes $\Gamma_{12} = \sqrt{\Gamma_{1D,1}\Gamma_{1D,2}} \exp(-i\Delta kd)$, where $\Delta k = \sqrt{\varepsilon_{\text{eff}}}\delta/c$. The first-order correction to the correlated decay (Δkd) is approximately 0.02 in our experiment and may be safely ignored, so that $\Gamma_{12} \approx \sqrt{\Gamma_{1D,1}\Gamma_{1D,2}}$. (For our experiment, $\sqrt{\varepsilon_{\text{eff}}} = 2.6$, $\delta = 2\pi \times 17$ MHz, $c = 3 \times 10^8$ m/s, $d = 18.2$ mm. Here, $\sqrt{\varepsilon_{\text{eff}}}$ is the refractive index and ε_{eff} is the effective permittivity.) If we additionally take the assumption that $\Gamma_{1D,1} = \Gamma_{1D,2}$, the Liouvillian in Eq. (B4) simplifies to

$$\mathcal{L}\rho = \Gamma_{1D}\mathcal{D}[\hat{\sigma}_1 + \hat{\sigma}_2]\rho, \quad (\text{B9})$$

which may be rewritten straightforwardly as

$$\mathcal{L}\rho = 2\Gamma_{1D}\mathcal{D}[|gg\rangle\langle T| + |T\rangle\langle ee|]\rho. \quad (\text{B10})$$

The simplified Hamiltonian [Eq. (B8)] and Liouvillian [Eq. (B10)] are illustrated in the left subpanel of Fig. 1(b). The triplet state $|T\rangle$ is superradiant and decays at rate $2\Gamma_{1D}$ to the ground state $|gg\rangle$. The singlet $|S\rangle$ has no decay but exchanges population with the triplet at rate $-\delta$. We note that here we have considered the case in which the qubit separation $d = m\lambda$. For qubit separations of $d = \lambda/2 \pm m\lambda$, the singlet and triplet are exchanged ($|S\rangle$ decays directly to $|gg\rangle$).

2. Dark-state formation

In our experiment, the interplay between drive, detuning, and decay results in the stabilization of a pure entangled state that is dark to the waveguide. In this appendix, we detail sufficient conditions for the formation of the dark state and discuss their physical meaning, closely following Refs. [34,35,43]. The conditions for the existence of a pure dark stationary state $|\Psi\rangle$ are as follows:

- (1) $|\Psi\rangle$ is annihilated by the collective jump operators (or, equivalently, $|\Psi\rangle$ exists in the null space of the collective jump operators). $c_{R,L}|\Psi\rangle = 0$. This condition ensures that $|\Psi\rangle$ does not decay to the waveguide output ports and is therefore “dark.”
- (2) $|\Psi\rangle$ is an eigenstate of the Hamiltonian. $\hat{H}|\Psi\rangle = E|\Psi\rangle$. This condition ensures stationarity.

The collective jump operators for qubits coupled to a waveguide are given by $c_R = \sum_i e^{ikx_i}\hat{\sigma}_i$ and $c_L = \sum_i e^{-ikx_i}\hat{\sigma}_i$, corresponding to collective decay to the right and left output ports. Here, k is the wave vector at the drive frequency ($k = n\omega/c$) and x_i is the position of qubit

i . We note that these jump operators are valid in the regime in which $\omega \approx \omega_1 \approx \omega_2$. If the waveguide dissipation rates Γ_{1D} are small compared to the qubit frequencies (ω_1 and ω_2) and the interqubit separation d does not greatly exceed a wavelength, variations in phase shift due to different frequencies are negligible [73]. Hence, the interference effects discussed in Appendix C remain valid.

We first consider condition (1), that $c_L|\Psi\rangle = c_R|\Psi\rangle = 0$. For the case of two qubits coupled to a waveguide, the jump operators may be written as $c_R = \hat{\sigma}_1 + e^{ikd}\hat{\sigma}_2$ and $c_L = \hat{\sigma}_1 + e^{-ikd}\hat{\sigma}_2$, where $d = |x_2 - x_1|$ is the qubit separation. The dissipators corresponding to these operators are $(\Gamma_{1D}/2)\mathcal{D}[c_{R,L}]\rho$. We note that for a qubit separation of $d = \lambda$, these dissipators sum to the Liouvillian of Eq. (B9). In general, the null space of $c_{R,L}$ consists of $|gg\rangle$ and $|\Psi_{R,L}\rangle = (|ge\rangle - e^{\pm ikd}|eg\rangle)/\sqrt{2}$. The state $|\Psi_{R,L}\rangle$ may be interpreted as the collective qubit state that results in the destructive interference of waveguide emission in the right (left) direction. For arbitrary qubit separation d , no state other than $|gg\rangle$ satisfies the destructive interference condition in both waveguide directions. However, when $d = m\lambda$ (or $d = \lambda/2 + m\lambda$) for integer m , the singlet (triplet) $|S, T\rangle = (|ge\rangle \mp |eg\rangle)/\sqrt{2}$ will be annihilated by both jump operators simultaneously, satisfying (1). We emphasize here the importance of precise control of the phase delay between qubits to achieve destructive interference to both waveguide ports. For our experiment, flux tuning the qubit frequencies allows us to tailor the phase delay *in situ*.

While $|gg\rangle$ and $|S\rangle$ annihilate both jump operators for $d = m\lambda$, neither are eigenstates of the Hamiltonian [Eqs. (2) and (B8)]. We note here that for arbitrary qubit detunings (δ_i) and Rabi drive frequencies (Ω_i), it is not possible to find an eigenstate of the Hamiltonian within the considered subspace. However, letting $\Omega_1 = \Omega_2$ and $\delta_1 = -\delta_2$ is sufficient to obtain a “dark” eigenstate by combining $|gg\rangle$ and $|S\rangle$. This state is given here [and in Eq. (3)] by

$$|D\rangle = \frac{|gg\rangle + \alpha|S\rangle}{\sqrt{1 + \alpha^2}}. \quad (\text{B11})$$

Here, the coherent drive, waveguide dissipation, and detunings all destructively interfere to remove coherent interactions between $|D\rangle$ and the rest of the state space. The parameter $\alpha = \Omega/\sqrt{2}\delta$ sets the singlet fraction (defined here as $\alpha^2/(1 + \alpha^2)$). For large Rabi drives, $|D\rangle$ asymptotically approaches the Bell state $|S\rangle$. By expressing the orthogonal state to $|D\rangle$ in the dark subspace, we may obtain intuition for the population dynamics. This orthogonal state is denoted as $|B\rangle$ and is given by

$$|B\rangle = \frac{\alpha|gg\rangle - |S\rangle}{\sqrt{1 + \alpha^2}}. \quad (\text{B12})$$

We observe that the ground state $|gg\rangle$ may be reexpressed as $|gg\rangle = (|D\rangle + \alpha|B\rangle)/\sqrt{1 + \alpha^2}$, allowing us to reexpress

the Liouvillian in Eq. (B10) as

$$\mathcal{L}\rho = 2\Gamma_{1D}\mathcal{D}\left[\frac{1}{\sqrt{1+\alpha^2}}|D\rangle\langle T| + \frac{\alpha}{\sqrt{1+\alpha^2}}|B\rangle\langle T| + |T\rangle\langle ee|\right]\rho. \quad (\text{B13})$$

This yields the effective decay (pumping) rates into $|D\rangle$ and $|B\rangle$ from $|T\rangle$:

$$\gamma_{\text{eff},D} = \frac{1}{1+\alpha^2} \times 2\Gamma_{1D} = \frac{2\Gamma_{1D}}{1+\Omega^2/2\delta^2}, \quad (\text{B14})$$

$$\gamma_{\text{eff},B} = \frac{\alpha}{1+\alpha^2} \times 2\Gamma_{1D} = \frac{2\Gamma_{1D}\Omega}{(1+\Omega^2/2\delta^2)\delta\sqrt{2}}. \quad (\text{B15})$$

Equation (B14) is given as Eq. (4) of the main text. Similarly reexpressing the Hamiltonian in Eq. (B8) yields an effective Rabi drive between $|B\rangle$ and $|gg\rangle$, given by

$$\Omega_{\text{eff},B} = \frac{1}{\sqrt{1+\frac{\Omega^2}{2\delta^2}}} \left(\frac{\Omega^2 + 2\delta^2}{2\delta} \right). \quad (\text{B16})$$

These decay and Rabi rates are illustrated in the right subpanel of Fig. 1(b). Here, we note the trade-off between fidelity of the stationary state to $|S\rangle$ (which increases with $\alpha/(1+\alpha^2)$) and the decay rate into the dark state (which increases with $1/(1+\alpha^2)$). This trade-off is typical of driven-dissipative stabilization schemes [22].

APPENDIX C: INELASTIC SCATTERING OF SUBRADIANT STATE

Resonance fluorescence measurements of the subradiant state ($|S\rangle$) are fitted to master-equation simulations, following Eq. (B1) with slight modifications. First, the qubit-drive detuning is set to zero ($\delta_i = 0$) in Eq. (B2). Next, internal loss and dephasing terms are added to the Liouvillian, given by

$$\mathcal{L}_{\text{int}}\rho = \sum_{i=1,2} \Gamma_{\text{int},i} \mathcal{D}[\hat{\sigma}_i]\rho \quad (\text{C1})$$

$$\mathcal{L}_{\phi}\rho = \sum_{i,j=1,2} \frac{\Gamma_{\phi,ij}}{2} \mathcal{D}[\hat{\sigma}_{z,i}, \hat{\sigma}_{z,j}]\rho. \quad (\text{C2})$$

Here, $\Gamma_{\phi,ii}$ is the dephasing of qubit i and $\Gamma_{\phi,ij} = \Gamma_{\phi,ji} = \Gamma_{\phi,\text{corr}}$ is the correlated dephasing. Correlations between qubit dephasing can arise when multiple qubits are coupled to a single noise source, such as a global magnetic field [27]. The total simulated Liouvillian accounts for waveguide decay [Eq. (B4)], internal losses, and dephasing ($\mathcal{L}_{\text{tot}}\rho = \mathcal{L}\rho + \mathcal{L}_{\text{int}}\rho + \mathcal{L}_{\phi}\rho$). The two-time correlation function then gives the power spectrum of the output

radiation field,

$$S(\omega) = \text{Re} \int_0^\infty \frac{d\tau}{\pi} e^{i\omega\tau} \langle c_R^\dagger(t) c_R(t+\tau) \rangle, \quad (\text{C3})$$

where c_R is the collapse operator ($c_R = \hat{\sigma}_1 + e^{ikd}\hat{\sigma}_2$), as defined in Appendix B. To reduce the number of free parameters in the fitted simulations, we set $\Gamma_{\text{int},1} = \Gamma_{\text{int},2}$ and $\Gamma_{\phi,11} = \Gamma_{\phi,22}$. The fitted parameters are $\Gamma_{\text{int}} = 0$, $\Gamma_{\phi} = 174 \pm 24$ kHz and $\Gamma_{\phi,\text{corr}} = 127 \pm 85$ kHz, as shown in the lower subpanel of Fig. 2(c). We note that following the treatment given in Ref. [27], the decay lifetime (T_1) of the subradiant state may be approximated as $T_1 = 1/(\Gamma_{\text{int}} + \Gamma_{\phi} - \Gamma_{\phi,\text{corr}})$ in the case of a large Purcell factor. This relation yields an estimate for $T_1 = 3.4 \mu\text{s}$, which greatly exceeds the single-qubit lifetimes of ≈ 16 ns (see Appendix D).

APPENDIX D: LIFETIME MEASUREMENT OF AN INDIVIDUAL QUBIT AND THE SUBRADIANT STATE

The individual-qubit and resonant-subradiant-state lifetimes are presented in Fig. 2(d). To measure the single-qubit lifetimes, individual qubits are excited via the waveguide with a constant π pulse. The qubit emission is demodulated (see Appendix E 1) using an 80-ns time window after a variable wait time τ and $\langle \hat{\sigma}^\dagger \hat{\sigma} \rangle$ is calculated. The individual-qubit T_1 lifetimes are $T_1 = 16.6 \pm 0.6$ ns for qubit 1 and $T_1 = 16.0 \pm 1.9$ ns for qubit 2.

The subradiant-state lifetimes are measured by exciting the singlet state ($|S\rangle = |eg\rangle - |ge\rangle$) with a constant π pulse. For an interqubit separation of λ ($\ell = \lambda$), driving through the waveguide can only excite the superradiant triplet state ($|T\rangle = |eg\rangle + |ge\rangle$). To excite the singlet state, XY lines are used to drive qubits out of phase simultaneously. After a variable wait time τ , the ground-state ($|gg\rangle$) population is then measured by state-dependent scattering [28]. In this scheme, if the ground state is populated, photons are scattered between $|gg\rangle$ and $|T\rangle$, reducing the transmission amplitude. Scattering results in unit transmission if the system is fully excited to $|S\rangle$. Fits to exponential decay profiles are used to extract lifetimes. The extracted T_1 lifetime for the singlet state is $T_1 = 910 \pm 47$ ns. We note here the discrepancy between this measurement result and the estimated T_1 lifetime from the inelastic scattering measurements ($T_1 = 3.4 \mu\text{s}$). We attribute this discrepancy to frequency shifts of the individual qubits over multiple days. The measured lifetimes of the subradiant state are crucially dependent on the individual-qubit frequencies due to the interference required to protect the state from decay; frequency jitter can, therefore, strongly affect lifetimes. Despite these discrepancies, the measured and estimated lifetimes of the subradiant state greatly exceed those of individual qubits, which are limited to ≈ 16 ns.

APPENDIX E: STATE TOMOGRAPHY

1. Measurement of qubit moments

Most superconducting qubits use a dedicated resonator for readout using single-shot dispersive readout [74]. Due to the nature of our experiment, however, the qubits are strongly coupled to a separate waveguide. Hence, without the use of a tunable coupler between the qubits and the waveguide, the qubit would mostly be decaying into this common waveguide, limiting the fidelities of the readout that we can achieve. Additionally, unless carefully designed, a readout resonator can act as another source of dissipation for the qubits, thus inhibiting the formation of a truly dark state. We instead use the strong coupling of the qubits to the common waveguide to perform our readout by means of field emission tomography, using techniques similar to those presented in Ref. [75]. As shown there, a direct mapping exists between the field emitted by a qubit and its state. This mapping is used to perform quantum state tomography on the two qubits. Following Ref. [75], the input-output relation for two qubits coupled to the same waveguide is given by

$$\begin{aligned} \hat{a}_{\text{out}}(t) = & \hat{a}_{\text{in}}(t) + e^{-i\omega_1 t_1} \sqrt{\frac{\Gamma_{1\text{D},1}}{2}} \hat{\sigma}_1(t) \\ & + e^{-i\omega_2 t_2} \sqrt{\frac{\Gamma_{1\text{D},2}}{2}} \hat{\sigma}_2(t), \end{aligned} \quad (\text{E1})$$

where $\hat{\sigma}_{1,2}$ are the qubit annihilation operators, $\Gamma_{1\text{D},1,2}$ are the decay rates of the respective qubits to the waveguide, and $t_{1,2}$ represent the time of flight to the qubits. \hat{a}_{out} and \hat{a}_{in} represent the output and input propagating modes in the waveguide (this is for only one propagation direction; a similar equation exists for the opposite direction). Clearly, measuring the output field of the waveguide can also be used to gain information of the state of the qubits. In fact, it can be used to determine the exact state of the qubits just before they begin emitting into the waveguide.

To see this, consider the case of a single qubit at a frequency ω_q the time-dependent annihilation operator of which is given by $\hat{\sigma}(t)$. The output field in this case, in the absence of any drive, is given by $\hat{a}_{\text{out}}(t) = \sqrt{\Gamma_{1\text{D}}/2} \hat{\sigma}(t) + \hat{a}_{\text{in}}(t)$, where $\hat{a}_{\text{in}}(t)$ is the vacuum. For a qubit naturally decaying into a waveguide, $\hat{\sigma}(t)$ evolves as $e^{-\Gamma_{1\text{D}} t/2} \hat{\sigma}(0) e^{-i\omega_q t}$, where $\Gamma_{1\text{D}}$ is the coupling to the waveguide. Now consider the integral

$$\hat{\sigma} = \int dt f(t) \hat{a}_{\text{out}}(t) e^{i\omega_q t}, \quad (\text{E2})$$

where $f(t)$ represents a weighting function to give a higher weight to times at which $\hat{a}_{\text{out}}(t)$ is larger. This is known as temporal mode matching and Eq. (E2) is a continuous version of what actually happens during demodulation of the output field during the experiment (see Appendix E2).

By choosing $f(t) = \sqrt{2\Gamma_{1\text{D}}} e^{-\Gamma_{1\text{D}} t/2} \Theta(t)$, where $\Theta(t)$ is the Heaviside step function, one can show that the integral $\hat{\sigma}$ reduces to simply $\hat{\sigma}(0)$, thus recovering the state of the qubit just before the emission began (our choice of $f(t)$ contains an additional $\sqrt{2}$ factor as compared to previous work, because qubits are side coupled rather than end coupled to the waveguide) [76]. Mode matching is done to maximize the detection efficiency. Thus, any choice of $f(t)$ still retains all the statistical properties of $\hat{\sigma}$ and can be used for the measurement at the cost of a possibly decreased signal-to-noise ratio (SNR). We henceforth use $\hat{\sigma}$ to denote the incoming mode but it is equivalent to the state of the qubit at the start of the emission.

Prior to being detected, the field $\hat{a}_{\text{out}}(t)$ passes through a linear amplification chain with a net gain of G , usually on the order of many tens of decibels. This is because the actual detection is done using analog-to-digital converters that have a minimum voltage threshold, which is generally much higher than that of a single microwave photon. Because of the amplification, there is some inevitable noise added as well [46,77] and hence what is actually detected is given by (in the limit of $G \gg 1$), $\hat{S} = \sqrt{G}(\hat{\sigma} + \hat{h}^\dagger)$, with \hat{h} representing the added noise. We discuss how we calculate G in Sec. E3. For now, consider the measurement of $\hat{S} = \hat{\sigma} + \hat{h}^\dagger$. We are primarily interested in finding the moments of $\hat{\sigma}$ and hence we need to properly account for the noise \hat{h} . This can be done by considering the binomial expansion of any moment of \hat{S} :

$$\langle \hat{S}^{\dagger n} \hat{S}^m \rangle = \sum_{i=0}^n \sum_{j=0}^m \binom{n}{i} \binom{m}{j} \langle \hat{\sigma}^{\dagger i} \hat{\sigma}^j \rangle \langle \hat{h}^{n-i} \hat{h}^{\dagger m-j} \rangle. \quad (\text{E3})$$

Here, the underlying assumption is that the noise is uncorrelated with the signal. This equation can then be used to generate a system of equations that can be used to recover the moments of $\hat{\sigma}$ instead, given that we know the moments of \hat{h} . To calculate the latter, we need to perform a measurement \hat{S}_0 with the signal mode $\hat{\sigma}$ in vacuum, such that all the moments of $\hat{\sigma}$ are 0, except for the zeroth order. This gives

$$\langle \hat{h}^n \hat{h}^{\dagger m} \rangle = \langle \hat{S}_0^{\dagger n} \hat{S}_0^m \rangle, \quad (\text{E4})$$

which can then be used to calculate the required moments of $\hat{\sigma}$.

Our detection protocol involves driving the two qubits for a certain duration through the waveguide, turning off the drive, and measuring the fields emitted by the two qubits. Since the two qubits are not very distant, the emitted fields are completely overlapped in the temporal domain. Instead, we note that the qubits are spectrally separated for our experimental settings and hence $\hat{\sigma}_1(t)$ and $\hat{\sigma}_2(t)$ rotate at different frequencies in Eq. (E1). This allows

us to use a frequency-multiplexed version of the above protocol.

Experimentally, a heterodyne detection in the microwave domain involves using an IQ mixer to down-convert from rf to a frequency range that can be digitized by an analog-to-digital converter (ADC). This sampled version of the field can then be demodulated (along with weights for the temporal mode matching) at the appropriate frequency to obtain an I, Q pair. This I, Q pair represents the two orthogonal quadratures of the detected field S , such that $S = I + iQ$, at the demodulated frequency. But once the signal has been down-converted and digitized, we can demodulate the signal at two different frequencies simultaneously to obtain two I, Q pairs representing \hat{S}_1 and \hat{S}_2 . These are then related to the two qubits $\hat{\sigma}_1$ and $\hat{\sigma}_2$ and two noise modes \hat{h}_1 and \hat{h}_2 in the same way that S is related to $\hat{\sigma}$ and \hat{h} , i.e.,

$$\begin{aligned}\hat{S}_1 &= \hat{\sigma}_1 + \hat{h}_1^\dagger, \\ \hat{S}_2 &= \hat{\sigma}_2 + \hat{h}_2^\dagger.\end{aligned}\quad (\text{E5})$$

The moments of the individual modes $\hat{\sigma}_1$ and $\hat{\sigma}_2$ can then be found in the same way as for $\hat{\sigma}$. The measurements for \hat{h}_1 and \hat{h}_2 are done by measuring \hat{S}_{01} and \hat{S}_{02} , where there is no signal mode. The cross-moments such as $\hat{\sigma}_1^\dagger \hat{\sigma}_2$ can also be found by calculating the cross-correlations between \hat{S}_1 and \hat{S}_2 . For example,

$$\begin{aligned}\langle \hat{S}_1^\dagger \hat{S}_2 \rangle &= \langle (\hat{\sigma}_1^\dagger + \hat{h}_1)(\hat{\sigma}_2 + \hat{h}_2^\dagger) \rangle \\ &= \langle \hat{\sigma}_1^\dagger \hat{\sigma}_2 \rangle + \langle \hat{h}_1 \hat{h}_2^\dagger \rangle + \langle \hat{\sigma}_1^\dagger \hat{h}_2^\dagger \rangle + \langle \hat{h}_1 \hat{\sigma}_2 \rangle \\ \implies \langle \hat{\sigma}_1^\dagger \hat{\sigma}_2 \rangle &= \langle \hat{S}_1^\dagger \hat{S}_2 \rangle - \langle \hat{h}_1 \hat{h}_2^\dagger \rangle - \langle \hat{\sigma}_1^\dagger \rangle \langle \hat{h}_2^\dagger \rangle - \langle \hat{h}_1 \rangle \langle \hat{\sigma}_2 \rangle,\end{aligned}$$

again under the assumption that the noise modes $\hat{h}_{1,2}$ are uncorrelated with the signal modes $\hat{\sigma}_{1,2}$.

2. Mode-matched filtering

Our field-tomography protocol recovers the qubit state by heterodyne detection of the field emitted into the waveguide. A finite time window (80 ns) is sufficient to capture the qubit emission ($T_1 \approx 16$ ns) and the emitted signal is subsequently down-converted with an IQ mixer to an intermediate frequency (IF) and digitized. The digitized signal ($\tilde{I} + i\tilde{Q}$) is then demodulated to obtain the field; the digital demodulation is detailed in the following expression:

$$S = I + iQ = \sum_n f[n](\tilde{I}[n] + i\tilde{Q}[n])e^{-i\omega_{\text{IF}}n\tau}. \quad (\text{E6})$$

Here, S corresponds to the measured field, n is the index, τ is the time resolution of our acquisition unit, and ω_{IF} is

the IF. $f[n]$ is the mode-matched filter function [discussed previously as $f(t)$ in Appendix E 1 and Eq. (E2)] and is the focus of the following discussion.

In our experiments, qubits are driven via the waveguide; drives are turned off just prior to the start of the measurement window. We note that in this discussion, the qubit and drive tone are detuned at the same settings as the dark-state experiment [for details, see Fig. 3(a) and Table I]. However, we find that artifacts of the drive are present in the measurement window—mainly due to drive-pulse dispersion and drive reflections. First, the dispersion of the drive pulse leaks into the measurement window. Second, repeated reflections of the drive at microwave connections in the measurement chain create delayed copies of drive pulses. In our experiment, we measure pulse dispersion and reflections in the qubit-emission window that is ≈ 20 dB lower than applied waveguide drives. Parasitic artifacts from the drive are within ≈ 5 dB of the power emitted from qubits and overlap temporally with the emission of interest. This effect is further exacerbated by the large qubit dissipation rate into the waveguide and the concomitant short emission duration ($\Gamma_{1D}/2\pi \approx 10$ MHz, $T_1 \approx 16$ ns). The majority of qubit emission is contained in the first 16 ns of the measurement window, which is most susceptible to the discussed parasitic effects. Capturing this drive signal in addition to qubit emission can potentially cause undesired correlations between the measured and background signals, S and S_0 , compromising the measurement fidelity [see Eqs. (E3) and (E5)].

To overcome this problem, we optimize the mode-matching function $f[n]$ to maximize the measured qubit emission while rejecting the parasitic drive signal in the measurement window. In other words, $f[n]$ is optimized to be orthogonal to parasitic artifacts of the drive. For this purpose, we measure ten averaged samples of single-qubit emission following a 100-ns drive pulse, denoted as S_1 . The state corresponding to S_1 is the steady state of the qubit of interest under a detuned coherent drive, as is evident in Figs. 6(b) and 6(c). We use the same qubit-drive detuning as in the stabilization experiment and the adjacent qubit is flux tuned away (≈ 1 GHz). Each sample contains 10^5 shots. Multiple averaged samples are used to mitigate the effects of fluctuations in gain or qubit emission over time. We repeat this measurement with the qubit detuned away, such that the measurement window only captures the parasitic drive (denoted as S_0) and no qubit signal. We then use nonlinear least-squares optimization to minimize the following loss function over the ten samples and remove the parasitic drive from the qubit signal:

$$L_{\text{bkg}}(f[n]) = \frac{|S_0|}{|S_1 - S_0|}. \quad (\text{E7})$$

Here, minimizing $|S_0|$ in the numerator orthogonalizes the filter function $f[n]$ with respect to the parasitic

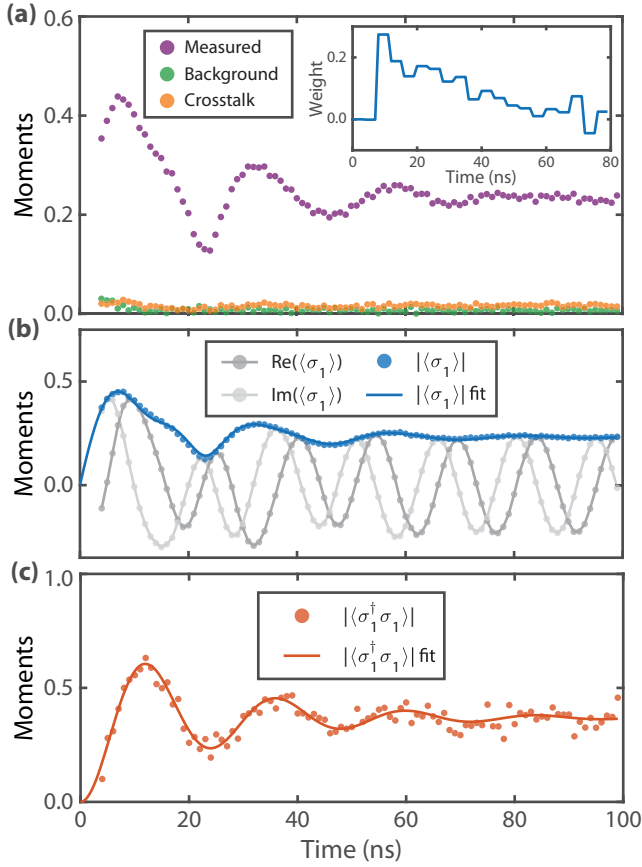


FIG. 6. The state tomography of an individual qubit. (a) The measured field quadrature of qubit 1 at the same detuned setting as Fig. 2(a), with qubit 2 flux tuned away (purple, S_1). The measured background field with both qubits flux tuned away (green, background, S_0). The measured field at the same detuned setting as Fig. 2(a), with qubit 1 flux tuned away (orange, crosstalk, S_2). The background and crosstalk are minimal compared to the signal. The inset shows the mode-matched envelope of qubit 1 (blue) and the ideal exponential decay envelope (red). The envelope maximizes the signal from the qubit while rejecting noise and crosstalk sources. (b) The background-subtracted field and (c) photon number of qubit 1 measured using mode-matched filtering, under a detuned drive [same setting as Fig. 2(a)]. Fits to master-equation simulations yield $\text{Gain} = 6.3 \pm 0.1 \times 10^5$.

drive. However, because of the substantial temporal overlap between the parasitic drive and the qubit signal, simply minimizing $|S_0|$ significantly reduces the qubit signal. Therefore, $|S_1 - S_0|$ is included in the denominator to maximize the output qubit signal. In Fig. 6(a), we show the result of this optimization for qubit 1. The purple plot denotes S_1 and the green plot denotes S_0 . When mode matching is applied, we see that S_0 is nearly zero over a range of drive-pulse durations. The optimized mode-matched temporal envelope for qubit 1 is shown in the inset to Fig. 6(a). We note that the filter function resembles an exponential decay with reduced weights in the first 8 ns

of the measurement window. This occurs because parasitic drive artifacts are localized in this short time window.

The steps detailed are sufficient to remove parasitic drive artifacts from the measurement window. Another source of noise in the qubit measurement arises when both qubits are measured simultaneously, as in our two-qubit dark-state tomography. In Fig. 3(a), we show the detuning profile of qubits 1 and 2 in the stabilization experiment. While the two qubits are separated by $\approx 3\Gamma_{1D}$ in frequency ($|\omega_{IF,1} - \omega_{IF,2}| > 3\Gamma_{1D}$), there is still the possibility for qubit demodulation to capture a ‘‘crosstalk’’ signal from the adjacent qubit. To remove this crosstalk, we simultaneously optimize for a second loss function ($L_{\text{total}} = L_{\text{bkg}} + L_{\text{cross}}$):

$$L_{\text{cross}}(f[n]) = \frac{|S_2 - S_0|}{|S_1 - S_0|}. \quad (\text{E8})$$

Here, the S_2 signal denotes the steady state of the adjacent qubit under a detuned drive, demodulated at the frequency of the qubit of interest. To obtain S_2 , ten qubit-emission samples are taken with the desired qubit detuned away and the adjacent qubit at the experimental setting. S_1 and S_0 are unchanged. Similar to the previous case, minimizing $|S_2 - S_0|$ (the adjacent qubit) rejects the parasitic crosstalk from the adjacent qubit. Maximizing $|S_1 - S_0|$ prevents the reduction of the signal of the desired qubit. In Fig. 6(a), we show the minimized crosstalk signal from qubit 2 (in orange), where qubit 1 is the qubit of interest.

In the case of perfect mode matching, the mode-matching efficiency is $\eta_F = 1$. For imperfect mode matching, $\eta_F < 1$; this has the effect of reducing the total detection efficiency and can be interpreted in a similar way to attenuation between the device and the first amplifier [76]. Ideally, qubit emission follows an exponentially decaying envelope and a corresponding exponential filter function provides perfect mode matching. In our experiment, the optimized filter functions are nonexponential in order to reject the parasitic noise sources discussed above. Our experimental mode-matching efficiency to qubit emission is therefore imperfect; we find $\eta_F = 0.59$ (0.50) for qubit 1 (2). The inset to Fig. 6(a) shows both the optimized (qubit-1) filter function (blue) and the corresponding ideal filter function (red). The mode-matching efficiency is calculated by taking the squared inner product between the normalized ideal and optimized filter functions. We note that using an ideal exponential filter function (where $\eta_F = 1$), we obtain ratios between the qubit and noise signal of $|S_1 - S_0|/|S_0| \approx 1$. This indicates the nontrivial effect of parasitic drive features in the absence of mode-matching optimization. On the other hand, the optimized filter function yields $|S_1 - S_0|/|S_0| \approx 20$ [see Fig. 6(a)].

Lastly, we verify that our mode-matching scheme does not affect the statistics of the measured moments by calibrating against master-equation simulations of single

qubits, which is discussed in Appendix E 3. We also note that when the parasitic drive and qubit emission are separable (i.e., nonentangled), tomography may alternatively be performed by directly subtracting the coherent displacement (caused by the drive) from the qubit signal.

3. Gain calibration and noise photon number

Qubit emission from the device passes through an amplifier chain and is then down-converted to an intermediate frequency, digitized, and digitally demodulated. The measured demodulated signal must be scaled properly to accurately recover the qubit state. We calibrate the gain of the measurement chain G by fitting master-equation simulations of a single qubit to demodulated emission, as shown in Figs. 6(b) and 6(c) for qubit 1. For this measurement, qubit 1 is flux tuned to the dark-state experiment setting (6.409 GHz) and a detuned drive (6.392 GHz) is applied. Digital demodulation is applied, with ω_{IF} corresponding to the qubit frequency. The obtained $|\langle \hat{\sigma}_1 \rangle|_{\text{meas}}$ and $|\langle \hat{\sigma}_1^\dagger \hat{\sigma}_1 \rangle|_{\text{meas}}$ are then fitted simultaneously to a master-equation simulation to obtain $|\langle \hat{\sigma}_1 \rangle| = \sqrt{G} |\langle \hat{\sigma}_1 \rangle|_{\text{meas}}$ and $|\langle \hat{\sigma}_1^\dagger \hat{\sigma}_1 \rangle| = G |\langle \hat{\sigma}_1^\dagger \hat{\sigma}_1 \rangle|_{\text{meas}}$. Gain calibration for qubits 1 and 2 yields $G = 6.3 \pm 0.1 \times 10^5$ and $G = 4.2 \pm 0.1 \times 10^5$, respectively. Note that the gain values include the contribution from mode matching. Asymmetry between the calibrated gain values is attributed to asymmetric crosstalk caused by the Fano line shape of each qubit. A qubit experiencing a crosstalk signal from the neighboring qubit will have a reduced gain G because mode-matched filtering will less efficiently capture the signal of the desired qubit.

The SNR of heterodyne field tomography depends on the number of noise photons injected at the first amplifier in the output chain, the losses between the output of the chip and the first amplifier, and also the mode-matching efficiency. All of this can be encapsulated by a single number, which is the effective noise photon number n_{eff} . The SNR scales with the order of the moment being measured as $(1 + n_{\text{eff}})^M$, where M is the order of the moment.

Our measured effective noise photon number is $n_{\text{eff}} = 122.4 (\pm 0.7)$ for qubit 1 and $n_{\text{eff}} = 76.2 (\pm 0.4)$ for qubit 2 (95% confidence intervals) [78]. The contributing factors to these values are noise injected by the first amplifier (13 photons), loss between the device and first amplifier (0.5 or ≈ 3 dB), the mode-matching efficiency (≈ 0.5), and photon loss due to bidirectional waveguide coupling (0.5). We extract the noise injected by the first amplifier (HEMT located at the 4-K stage) by referencing to a resonance fluorescence measurement of a single qubit. This measurement yields a noise photon number of $n_{\text{HEMT}} = 13$ photons and a temperature of $T_{\text{HEMT}} = 4.1$ K. We note that n_{eff} can be reduced using a near-quantum-limited amplifier [79].

4. Maximum-likelihood estimation

Once we have all the moments of the photonic modes emitted by the qubit (see Appendix E 1), we use the standard method of maximum-likelihood estimation (MLE) to obtain the density matrices for the two-qubit state [76,77]. Since we only have emission from the first excited state of the transmon (the second excited level is approximately 300 MHz away), we can work in the single-excitation sector for each mode. We can thus restrict our attention to the 16 moments of the form $A_j = (\hat{\sigma}_1^\dagger)^{n_1} \hat{\sigma}_1^{m_1} (\hat{\sigma}_2^\dagger)^{n_2} \hat{\sigma}_2^{m_2} \forall n_1, n_2, m_1, m_2 \in \{0, 1\}$.

Following Ref. [77], given a state ρ , the probability of measuring $\langle \bar{A}_j \rangle$ as the mean of N measurements of a particular moment A_j is given by

$$p(\langle \bar{A}_j \rangle | \rho) \propto e^{-|\langle \bar{A}_j \rangle - \text{Tr}(A_j \rho)|^2 / (v_j / N)}, \quad (\text{E9})$$

where v_j is the variance of the moment. For large enough N , the law of large numbers tells us that we can approximate v_j by the measured variance. One can then define the log of a likelihood function,

$$-\log \mathcal{L}(D | \rho) = \sum_{j=1}^{16} |\langle \bar{A}_j \rangle - \text{Tr}(A_j \rho)|^2 / (v_j / N), \quad (\text{E10})$$

where j enumerates all the different moments. This, along with the constraints that $\text{Tr}(\rho) = 1$ and $\rho > 0$, defines an objective function to be used for the minimization problem that finds the most likely density matrix for the given set of measured moments.

We calculate the fidelity of the extracted stabilized state to a Bell state $|\psi\rangle = (|eg\rangle + e^{i\phi}|ge\rangle) / \sqrt{2}$, without post-processing of the measured relative phase delay. Instead, ϕ is swept over a 2π range and the ϕ yielding maximum fidelity is used. This relative phase rotation corresponds to a virtual single-qubit Z rotation and does not affect the generated entanglement (concurrence).

To find the bounds on fidelity and concurrence, we perform MLE on resampled copies of the moments. We record the average of all the moments over 1×10^6 shots and perform this entire measurement 3000 times (a total of 3×10^9 averages). This gives us an approximately Gaussian histogram of 3000 values, from which we extract the variance and mean. We then resample each moment from a Gaussian with the corresponding parameters to reconstruct 1000 resampled copies. For each resampled copy, we perform MLE and calculate the fidelity and concurrence. The standard deviation can be calculated from this list of fidelities and concurrences and the 95% confidence interval is then bounded by the 25th and 975th elements of the sorted lists.

APPENDIX F: ANALYSIS OF THE DECOHERENCE SOURCES

We observe in Fig. 4(b) that the concurrences of the stabilized entangled state exceed the values predicted by qubit Purcell factors (approximately ten, extracted from fits to transmission traces). To investigate potential sources of this discrepancy, we perform measurements of qubit decoherence caused by interaction with the waveguide bath. In particular, we study the effects of the drive power.

Our dark-state stabilization protocol involves applying strong drives ($\Omega/\Gamma_{1D} > 1$) to the qubits via the waveguide. Previous studies have found that decoherence during the driven evolution of a qubit depends on the noise power spectral density (PSD) at the Rabi frequency, which has been shown to exhibit a $1/f^\alpha$ dependence [51,52,80–82]. We investigate the noise PSD by measuring the driven evolution of single qubits using Rabi noise spectroscopy [80] and a spin-locking (SL) protocol [51].

1. Driven evolution of a qubit

The decoherence of a qubit under driven evolution has noise contributions from the qubit frequency ω_q , the Rabi drive frequency Ω_R , and quasistatic noise [80]. We consider the evolution of a single qubit under a resonant drive, which is described by the following Hamiltonian in the laser frame, with $\delta = \omega_q - \omega_d = 0$:

$$\hat{H} = \frac{\delta}{2}\hat{\sigma}_z + \frac{\Omega_R}{2}\hat{\sigma}_y. \quad (\text{F1})$$

To understand our noise-spectroscopy measurement protocols, we invoke an analogy between the free and driven evolution of a qubit [51]. A freely evolving qubit revolves around the z axis of the Bloch sphere at a frequency δ (in the laser frame). The qubit will experience a longitudinal ($\Gamma_1 = 1/T_1$) and transverse decay ($\Gamma_2 = \Gamma_1/2 + \Gamma_\phi = 1/T_2$, where Γ_ϕ is pure dephasing) when subjected to the environment. When the qubit is driven on resonance in the y direction, the qubit state revolves about the y axis with the Rabi frequency Ω_R . In this case, the driven dynamics can be interpreted as a freely evolving spin quantized in the y -axis direction. In analogy with the case of the non-driven qubit, longitudinal ($\tilde{\Gamma}_1$) and transverse ($\tilde{\Gamma}_2$) decay rates may be defined (given below for a resonant drive): [52].

$$\tilde{\Gamma}_1 = \frac{1}{2}\Gamma_1 + \Gamma_\nu, \quad (\text{F2})$$

$$\tilde{\Gamma}_2 = \frac{3}{4}\Gamma_1 + \frac{1}{2}\Gamma_\nu. \quad (\text{F3})$$

Here, $\Gamma_\nu = \pi S_z(\Omega_R)$ is the pure dephasing under driven evolution, where $S_z(\Omega_R)$ is the noise PSD at the Rabi frequency Ω_R . ($\Gamma_\phi = \pi S_z(0)$ is the pure dephasing under

free evolution). By varying the qubit drive strength and measuring decoherence rates, the noise PSD $S_z(\Omega_R)$ may be extracted. We measure $\tilde{\Gamma}_2$ and $\tilde{\Gamma}_1$ in two independent experiments: driven Rabi spectroscopy and a modified SL protocol (respectively). We describe these experiments in the following sections.

2. Driven Rabi spectroscopy

To measure the Rabi oscillations, we directly drive the qubit via the waveguide with variable pulse durations (τ) and measure the emitted field to obtain the qubit state. The measurement-pulse protocol is shown in the inset of Fig. 7(a). For a qubit initially in the ground state $\langle\sigma_z\rangle(t=0) = -1$ and given $\Omega_R \geq |\Gamma_1 - \Gamma_2|/2$, the driven evolution may be solved analytically, yielding

$$\langle\sigma_x\rangle(\tau) = x_\infty - \left(\frac{\tilde{\Gamma}_2 x_\infty - \Omega_R}{\nu_R} \sin(\nu_R \tau) + x_\infty \cos(\nu_R \tau) \right) \times \exp(-\tilde{\Gamma}_2 \tau), \quad (\text{F4})$$

with $\langle\sigma_y\rangle(\tau) = 0$. Here, $\nu_R = \sqrt{\Omega_R^2 - (\Gamma_1 - \Gamma_2)^2/4}$ is the effective Rabi-oscillation frequency. The steady-state value of $\langle\sigma_x\rangle$ is $x_\infty = \Gamma_1 \Omega / (\Gamma_1 \Gamma_2 + \Omega^2)$ and the envelope decays at $\tilde{\Gamma}_2$. An example of the measured Rabi oscillations of qubit 2 is shown in Fig. 7(a), with a fit to Eq. (F4). In these fits, Γ_1 is set constant at 10.5 MHz (estimated from transmission traces; see Table I), while all other parameters are allowed to vary. We note here that we exclude quasistatic noise in our analysis [80], which manifests in nonexponential decay (a feature not observed in our experiment). Sweeping the drive power Ω_R from 10 to 37 MHz gives an approximate $1/f$ dependence for Γ_ϕ [and therefore $S_z(\Omega_R)$], shown in Fig. 7(c). The extracted Γ_ν values range from 0.1 to 1.1 MHz. We note that at drive powers above 37 MHz, the fitted Γ_ν values approach zero. This indicates that the driven Rabi measurement is not sensitive enough to detect $\Gamma_\phi < 0.1$ MHz, because a large Γ_1 dominates the decay. This motivates the use of the spin-locking protocol discussed next.

3. Modified spin-locking protocol

We independently extract Γ_ν using a modified SL protocol discussed in Ref. [51], which measures longitudinal decay in the driven qubit frame ($\tilde{\Gamma}_1$). Previous studies have demonstrated more sensitive noise spectroscopy with the SL protocol, citing robustness against low-frequency fluctuations in the Rabi frequency (Ω_R) due to instrumentation and low-frequency qubit dephasing [51]. The protocol involves first using a resonant $\pi/2$ pulse in the x direction (on the Bloch sphere) to initialize a qubit state collinear with the y axis. This is immediately followed by a continuous $\pi/2$ phase-shifted drive in the y direction to begin

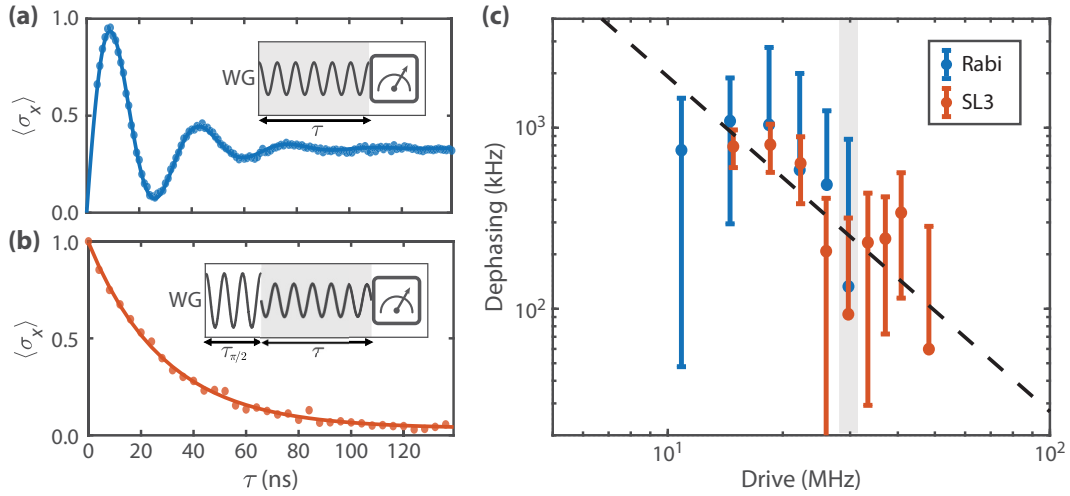


FIG. 7. The individual-qubit decoherence when driven via the waveguide. (a) The driven Rabi oscillations of qubit 2 with a drive of $\Omega_R/2\pi = 30$ MHz. The extracted $\Gamma_\phi = 133$ kHz. The inset shows the Rabi-spectroscopy pulse sequence. (b) The spin-locking-protocol decay signal for qubit 2, with a drive of $\Omega_R/2\pi = 30$ MHz. The extracted $\Gamma_\phi = 93$ kHz. The inset shows the spin-locking-protocol pulse sequence. (c) The extracted dephasing Γ_ν over a range of drive powers for the Rabi (blue) and spin-locking (SL, red) protocols, with 95% confidence intervals indicated by error bars. The dotted line indicates the fit of the spin-locking measurement dephasing versus the drive power to $1/f^\alpha$, yielding $\alpha = 1.85$. Data corresponding to (a) and (b) are shaded in gray.

the driven evolution. Ideally, the drive and qubit state are parallel, so that the qubit state relaxes to the center of the Bloch sphere at rate $\tilde{\Gamma}_1$. This pulse sequence is shown in the inset to Fig. 7(b). The qubit state is measured via waveguide emission as it decays. We note here that our measurement protocol does not include a second $\pi/2$ pulse used in Ref. [51] because we do not use a read-out resonator. An example of the exponential decay profile measured for qubit 2 is shown in Fig. 7(b). Fits to the relaxation include $\Gamma_1 = 10.5$ MHz as a fixed parameter and Γ_ν as a free parameter. The extracted Γ_ν ranges from 60 to 800 kHz over a range of Rabi frequencies from 15 to 48 MHz. A fit to the extracted Γ_ν reveals a $1/f^\alpha$ dependence with $\alpha = 1.85$.

4. Purcell factor under driven evolution

The observed reduction in Γ_ν at higher drive powers indicates that the true Purcell factor of our qubits is larger than approximately ten (extracted from VNA traces), which qualitatively explains the increase in concurrence observed in Fig. 4(b). However, extracted concurrences do not indicate monotonically increasing Purcell factors with the drive power [Fig. 4(b)], which would be expected for a purely $1/f^\alpha$ trend in dephasing. Instead, at low powers, concurrences indicate Purcell factors exceeding 30, while at high powers, Purcell factors range from 10 to 30. Previous studies [51] have reported Lorentzian “bump-like” features in the noise PSD attributed to coherent two-level system (TLS) fluctuators. While this could explain the above discrepancies, the large confidence bounds of the extracted Γ_ν values [Fig. 7(c)] preclude a quantitative conclusion. We also note that the driven evolution and

spin-locking measurements described in this appendix only probe the dephasing of *single* qubits. Correlated dephasing, which could potentially contribute to deviations in concurrence and fidelity, is not captured. We do not consider correlated dephasing in Fig. 4(c) because it is difficult to reliably extract this parameter at the large interqubit detuning used in the stabilization experiment.

APPENDIX G: NUMERICAL MODELING

We use a master-equation solver in QuTip [83,84] to simulate our system. We use the same Hamiltonian as in Appendix B but also include the third level (f) of transmons (see Appendix G 1). The simulation also includes dissipators for dephasing and intrinsic loss of the individual qubits (for the second level), as well as for correlated decay into the waveguide between the two transmons. Note that we do not include any waveguide-mediated interaction in the Hamiltonian, as discussed in Appendix B. The shaded regions in Figs. 3 and 4 have been found via these simulations, using different Purcell factors. The Purcell factor is varied by changing the intrinsic loss and dephasing rates of the individual transmons. Parameters such as the individual coupling rates of the qubits to the waveguide are set to match the fits of the experimental data at the operation frequencies, i.e., coupling rates of 8.7 MHz for qubit 1 and 10.5 MHz for qubit 2.

1. Effects of the e - f transition

An important aspect of the simulations has been the inclusion of the third level of the transmons. We have observed that while the third level does not significantly

impact the maximum achievable fidelities, it does affect the operation ranges for a given fidelity. As can be seen from Appendix B, for no dephasing and no intrinsic loss, the singlet fraction, which is directly related to the fidelity for a pure state, is only a function of the ratio of the detuning and the drive power. This would mean that increasing the drive strength for any detuning would help increase the fidelity of the steady state. In practice, this would also increase the settling time, which competes with any intrinsic loss or dephasing of the qubits. Hence there are optimal drive-to-detuning ratios for a true two-level system model. This can be seen in Fig. 8(a), which shows results from a simulation with a Purcell factor of 200 for the qubits and equal couplings of 10 MHz to the waveguide. We perform a sweep for various drives and detunings but do not include the $e-f$ transition for Fig. 8(a). Here, we can clearly see regions of high fidelity, even for high drive powers. In contrast, once we include the $e-f$ transition [Fig. 8(b)], the parameter space with high fidelities is restricted. Increasing the drive power for a given drive-to-detuning ratio does not necessarily help in this case. We expect that this has to do with the $e-f$ transition allowing the system to escape out of the relevant Hilbert space. Since the third level is populated more for higher drive powers, we see a clear deviation from the two-level system model at these drives.

2. Choice of detunings

As discussed in the main text, qubit-drive detunings (δ_1 and δ_2) must be selected to maximize the fidelities; we must properly balance a large singlet fraction ($|\alpha|^2/(1+|\alpha|^2)$) and a stabilization rate ($\gamma_{\text{eff},D}$). In the absence of intrinsic qubit decoherence (Γ'), smaller qubit-drive detunings δ correspond to an increased singlet fraction and dark-state fidelities at the cost of reduced stabilization rates. For finite Purcell factors ($\Gamma' > 0$), the maximum fidelities instead correspond to nonzero detunings, because the stabilization rate must be increased to compete with qubit decoherence, causing leakage out of $|D\rangle$. This is captured in the master-equation simulations shown in Fig. 9. Simulations with experimental values of Γ_{1D} for both qubits show fidelities exceeding 60% over certain parameter regimes. Based on these simulations, we choose an initial point of 15 MHz for the detuning and then we experimentally sweep the detuning around this point to choose the point of highest fidelity. We finally choose a detuning of 17 MHz. Higher detunings require flux-tuning qubit 1 away from its flux sweet spot and could potentially reduce the Purcell factors, and hence our fidelities (Fig. 9 uses a constant Purcell factor of 20). Additionally, higher detuning would also require higher drive powers, resulting in more artifacts of the drive creeping into our readout and lowering the SNR (Appendix E 2). This is not an inherent limitation of the protocol, and it can even be avoided with the use of fast-flux lines, as also suggested in Appendix H.

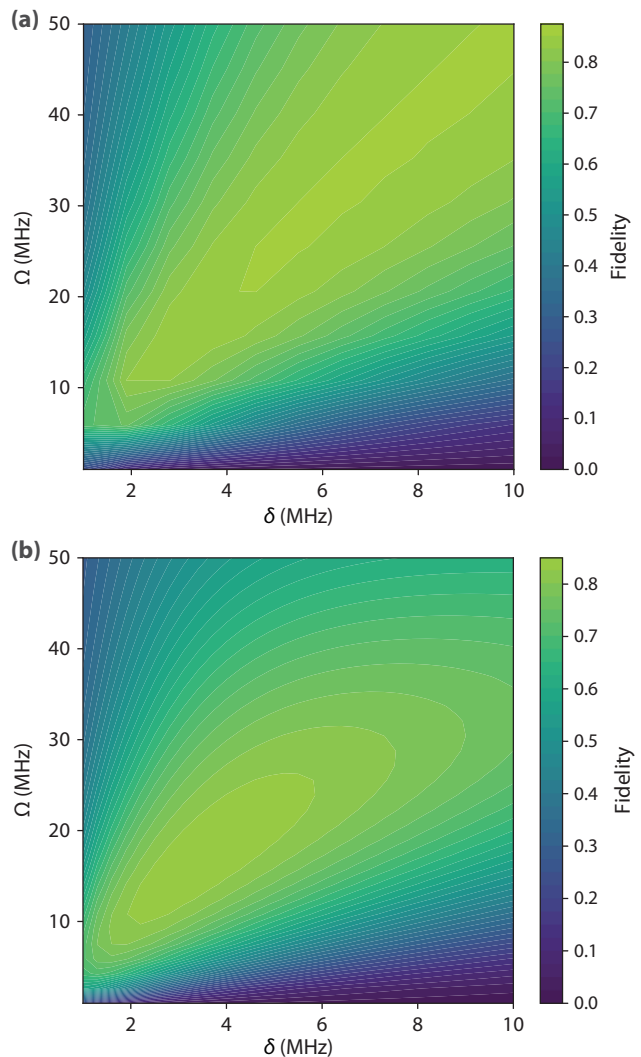


FIG. 8. Achievable fidelities for different parameter regimes of the drive strength (Ω) and the detunings (δ), (a) without the $e-f$ transition and (b) with the $e-f$ transition included in the master equation. Clearly, the inclusion of the third level makes a significant difference in the operational region, while the maximum fidelity is roughly the same (for more details of the simulation, see Appendix G 1).

APPENDIX H: ACHIEVABLE FIDELITIES IN FUTURE EXPERIMENTS

In this appendix, we discuss the challenges that we have faced in our experiment that have limited our fidelities. We will then discuss avenues to overcome these bottlenecks and use simulations to show that it is possible to even reach fidelities of over 90% with this driven-dissipative stabilization protocol and experimentally viable parameters for the transmons.

The first limitation of our experiment has, in fact, been the effect of the $e-f$ transition. As mentioned in Appendix G 1, the highest achievable fidelity is not very different between a true two-level system model and that of

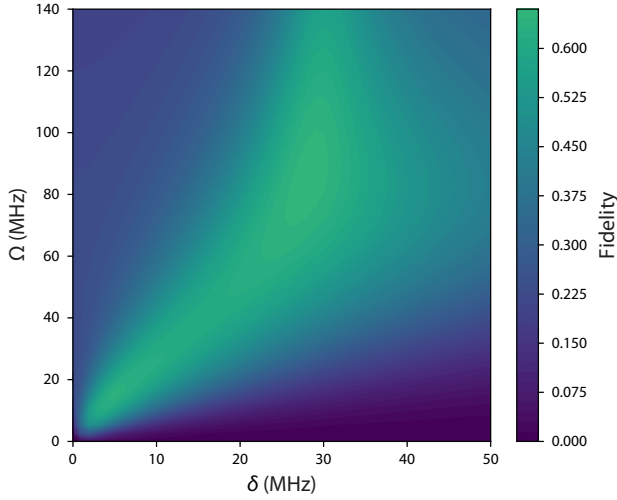


FIG. 9. The fidelities as a function of the drive and detunings for Γ_{1D} that we measure experimentally. We operate at $\delta = 17$ MHz, with varying powers. The simulation has been done with a Purcell factor of 20 on both qubits, with the extracted Γ_{1D} for the two qubits from the experiment.

a transmon but the operation point does change and tends to move toward lower detunings. While we could, in principle, use such an operation point, the effects of crosstalk and drive-pulse dispersion (described in Appendix E 2) have been more pronounced at lower detuning and would have affected our measurements.

This effect could be avoided by using fast flux lines to tune the qubits far enough after state preparation to conduct the measurement. Alternatively, dedicated readout resonators with other architectural changes to the design could be used as well. In particular, the coupling of the qubits to the waveguide would have to be tunable. Without a tunable coupling, the qubits would emit into the waveguide during readout, which would reduce the fidelities of the measurement. The fact that the qubits are strongly coupled to the waveguide (order of tens of megahertz to increase the Purcell factors) would reduce the fidelities further, since they impose stringent limitations on the duration of the dispersive readout pulse.

Another limitation to our experiment has been the imbalance in Γ_{1D} of the two qubits at their operation points due to impedance mismatches in measurement cabling causing Fano in the waveguide response. While this in itself is not very detrimental to the fidelities, having a common drive and different Γ_{1D} causes a difference in the Rabi drives that each qubit sees. This imbalance in drive strength can be shown to prevent the singlet state from being truly dark [43], thus reducing the fidelities. Our experiment has had an imbalance of around 4%, which, along with the limitation on detunings mentioned earlier, has reduced our maximum achievable fidelities by around

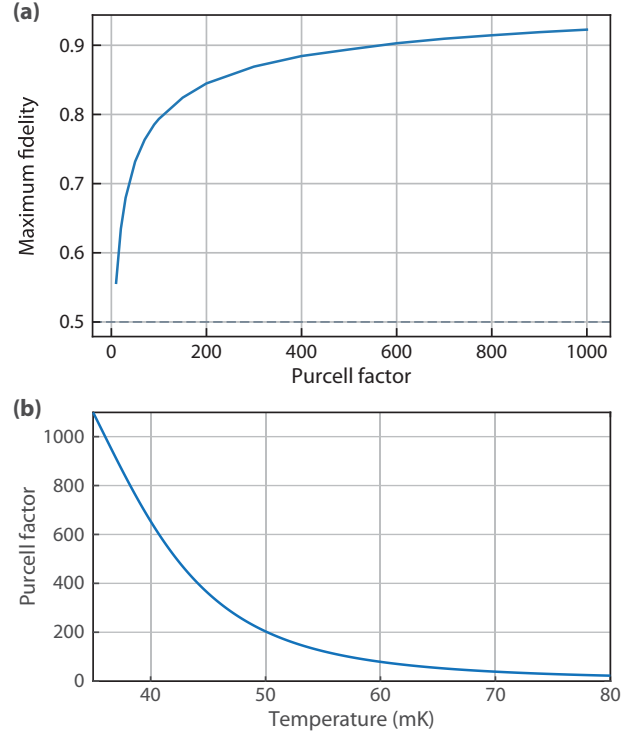


FIG. 10. The maximum achievable fidelities. (a) The achievable fidelities for different Purcell factors of the individual qubits. The dashed line marks the 50% threshold for entanglement. (b) Estimates of the maximum achievable Purcell factors under strong driving. The upper limit on the Purcell factor set by the waveguide temperature when dephasing is ignored, assuming internal losses of $\Gamma' = 6$ kHz. At 39 mK, $\Gamma_{1D}/\Gamma' = 730$.

6% [see the blue shaded region of Fig. 4(c)]. The previously mentioned design of having tunable couplers can help mitigate this effect, as the coupling rates would then be *in situ* tunable.

While these two challenges have affected our fidelities, the primary bottleneck in our experiment has, in fact, been the Purcell factor of our qubits ($P_{1D} = \Gamma_{1D}/\Gamma'$, $\Gamma' = 2\Gamma_2 - \Gamma_{1D} = \Gamma_{\text{int}} + 2\Gamma_\phi$). This sets an upper bound on the fidelities in our stabilization protocol. In Fig. 10(a), we show the maximum achievable fidelities as the Purcell factor is increased. From the measured transmission of our qubits, we estimate that our (undriven) Purcell factors are 10, which clearly limits our fidelities. Of course, in our protocol, the continuous driving of the qubits reduces the pure dephasing of the qubits (Appendix F 4) and, hence, we see higher concurrences and fidelities than that estimated by a Purcell factor of only 10.

We estimate that this scheme of generating entanglement can reach fidelities exceeding 90% (concurrence exceeding 0.86) for driven Purcell factors of 600 and above. To our knowledge, the highest reported Purcell factor for a qubit directly coupled to a waveguide is approximately 200 [27]. Meanwhile, state-of-the-art aluminum

transmons exhibit lifetimes of several hundred microseconds [85], which correspond to Purcell factors exceeding 1000. One of the causes of this apparent gap in performance is the thermal occupation of the waveguide in the former case. Qubits directly coupled to waveguides experience additional decoherence due to interaction with thermal photons residing in the photonic bath. This nonzero waveguide temperature degrades the Purcell factor. Again, for our stabilization protocol, strong drives mitigate this effect slightly due to a reduction in pure dephasing (discussed in Appendix F 4). Nevertheless, the finite waveguide temperature ultimately imposes an upper bound on the achievable Purcell factors. Following the master-equation treatment of Ref. [27], the Purcell factor in the presence of a finite waveguide temperature is $P_{1D} = \Gamma_{1D}/\Gamma'_{th}$, where Γ'_{th} is the intrinsic qubit decoherence and is defined as $\Gamma'_{th} = 2\Gamma_{2,th} - \Gamma_{1D}$ ($\Gamma_{2,th} = \Gamma_{1,th}/2 + \Gamma_{\phi}$, $\Gamma_{1,th} = (2\bar{n}_{th} + 1)\Gamma_1$, \bar{n}_{th} denotes bath occupancy).

As a side remark, at such high Purcell factors, it is also important to consider the precision with which we can control the qubit frequencies. For example, as mentioned in the main text, operating away from the center frequency ω (where the interqubit separation along the waveguide is equal to the wavelength) results in additional loss from the ideal dark state. For parameters close to our experiment, one can estimate a loss of around 100 kHz for a mismatch of 145 MHz between the drive frequency and the ideal center frequency. While this does not require extremely precise qubit-frequency control, it still does require *in situ* frequency control to overcome junction-fabrication disorder in fixed-frequency qubits. More importantly, as can be seen from Fig. 8, at sufficiently high Purcell factors, precision on the order of a few megahertz is definitely required for navigating the parameter space to attain the highest fidelities.

Using a reference measurement of Γ_1 for a separate qubit chip (without any coupling to a waveguide), we may estimate Γ' for the main device. This separate chip contains a qubit coupled to a readout resonator and undergoes a fabrication procedure identical to that for the main device. We measure $T_1 = 25.5 \pm 1 \mu\text{s}$ for the separate qubit device, corresponding to $\Gamma'/2\pi$ of 6 kHz. Previously reported waveguide temperatures have been as low as 39 mK [75]. At 39 mK, the Purcell factor is limited to 730 by the bath (for an estimate of $\Gamma'/2\pi = 6$ kHz), as shown in Fig. 10(b). This would enable us to reach a fidelity of 91% and a concurrence of 0.88 with a stabilization rate of 250 kHz.

-
- [1] H. J. Briegel, W. Dür, J. I. Cirac, and P. Zoller, Quantum repeaters: The role of imperfect local operations in quantum communication, *Phys. Rev. Lett.* **81**, 5932 (1998).
 [2] A. K. Ekert, Quantum cryptography based on Bell's theorem, *Phys. Rev. Lett.* **67**, 661 (1991).

- [3] S. Wehner, D. Elkouss, and R. Hanson, Quantum Internet: A vision for the road ahead, *Science* **362**, eaam9288 (2018).
 [4] D. Gottesman and I. L. Chuang, Demonstrating the viability of universal quantum computation using teleportation and single-qubit operations, *Nature* **402**, 390 (1999).
 [5] L. Jiang, J. M. Taylor, A. S. Sørensen, and M. D. Lukin, Distributed quantum computation based on small quantum registers, *Phys. Rev. A* **76**, 062323 (2007).
 [6] J. Eisert, K. Jacobs, P. Papadopoulos, and M. B. Plenio, Optimal local implementation of nonlocal quantum gates, *Phys. Rev. A* **62**, 052317 (2000).
 [7] C. Monroe, R. Raussendorf, A. Ruthven, K. R. Brown, P. Maunz, L. M. Duan, and J. Kim, Large-scale modular quantum-computer architecture with atomic memory and photonic interconnects, *Phys. Rev. A* **89**, 419 (2014).
 [8] S. Storz, *et al.*, Loophole-free Bell inequality violation with superconducting circuits, *Nature* **617**, 265 (2023).
 [9] Y. P. Zhong, H. S. Chang, K. J. Satzinger, M. H. Chou, A. Bienfait, C. R. Conner, É. Dumur, J. Grebel, G. A. Peairs, R. G. Povey, D. I. Schuster, and A. N. Cleland, Violating Bell's inequality with remotely connected superconducting qubits, *Nat. Phys.* **15**, 741 (2019).
 [10] L. M. Duan, M. D. Lukin, J. I. Cirac, and P. Zoller, Long-distance quantum communication with atomic ensembles and linear optics, *Nature* **414**, 413 (2001).
 [11] N. Roch, M. E. Schwartz, F. Motzoi, C. Macklin, R. Vijay, A. W. Eddins, A. N. Korotkov, K. B. Whaley, M. Sarovar, and I. Siddiqi, Observation of measurement-induced entanglement and quantum trajectories of remote superconducting qubits, *Phys. Rev. Lett.* **112**, 170501 (2014).
 [12] J. F. Poyatos, J. I. Cirac, and P. Zoller, Quantum reservoir engineering with laser cooled trapped ions, *Phys. Rev. Lett.* **77**, 4728 (1996).
 [13] F. Verstraete, M. M. Wolf, and J. I. Cirac, Quantum computation and quantum-state engineering driven by dissipation, *Nat. Phys.* **5**, 633 (2009).
 [14] M. B. Plenio, S. F. Huelga, A. Beige, and P. L. Knight, Cavity-loss-induced generation of entangled atoms, *Phys. Rev. A* **59**, 2468 (1999).
 [15] H. Krauter, C. A. Muschik, K. Jensen, W. Wasilewski, J. M. Petersen, J. I. Cirac, and E. S. Polzik, Entanglement generated by dissipation and steady state entanglement of two macroscopic objects, *Phys. Rev. Lett.* **107**, 080503 (2011).
 [16] M. J. Kastoryano, F. Reiter, and A. S. Sørensen, Dissipative preparation of entanglement in optical cavities, *Phys. Rev. Lett.* **106**, 090502 (2011).
 [17] Y. Lin, J. P. Gaebler, F. Reiter, T. R. Tan, R. Bowler, A. S. Sørensen, D. Leibfried, and D. J. Wineland, Dissipative production of a maximally entangled steady state of two quantum bits, *Nature* **504**, 415 (2013).
 [18] S. Shankar, M. Hatridge, Z. Leghtas, K. M. Sliwa, A. Narla, U. Vool, S. M. Girvin, L. Frunzio, M. Mirrahimi, and M. H. Devoret, Autonomously stabilized entanglement between two superconducting quantum bits, *Nature* **504**, 419 (2013).
 [19] F. Reiter, D. Reeb, and A. S. Sørensen, Scalable dissipative preparation of many-body entanglement, *Phys. Rev. Lett.* **117**, 040501 (2015).
 [20] M. E. Kimchi-Schwartz, L. Martin, E. Flurin, C. Aron, M. Kulkarni, H. E. Tureci, and I. Siddiqi, Stabilizing entanglement via symmetry-selective bath engineering in

- superconducting qubits, *Phys. Rev. Lett.* **116**, 240503 (2015).
- [21] Y. Liu, S. Shankar, N. Ofek, M. Hatridge, A. Narla, K. M. Sliwa, L. Frunzio, R. J. Schoelkopf, and M. H. Devoret, Comparing and combining measurement-based and driven-dissipative entanglement stabilization, *Phys. Rev. X* **6**, 011022 (2016).
- [22] T. Brown, E. Doucet, D. Ristè, G. Ribeill, K. Cicak, J. Aumentado, R. Simmonds, L. Govia, A. Kamal, and L. Ranzani, Trade off-free entanglement stabilization in a superconducting qutrit-qubit system, *Nat. Commun.* **13**, 3994 (2022).
- [23] S. Diehl, A. Micheli, A. Kantian, B. Kraus, H. P. Büchler, and P. Zoller, Quantum states and phases in driven open quantum systems with cold atoms, *Nat. Phys.* **4**, 878 (2008).
- [24] G. Morigi, J. Eschner, C. Cormick, Y. Lin, D. Leibfried, and D. J. Wineland, Dissipative quantum control of a spin chain, *Phys. Rev. Lett.* **115**, 200502 (2015).
- [25] J. T. Barreiro, M. Müller, P. Schindler, D. Nigg, T. Monz, M. Chwalla, M. Hennrich, C. F. Roos, P. Zoller, and R. Blatt, An open-system quantum simulator with trapped ions, *Nature* **470**, 486 (2011).
- [26] A. F. van Loo, A. Fedorov, K. Lalumière, B. C. Sanders, A. Blais, and A. Wallraff, Photon-mediated interactions between distant artificial atoms, *Science* **342**, 1494 (2013).
- [27] M. Mirhosseini, E. Kim, X. Zhang, A. Sipahigil, P. B. Dieterle, A. J. Keller, A. Asenjo-Garcia, D. E. Chang, and O. Painter, Cavity quantum electrodynamics with atom-like mirrors, *Nature* **569**, 692 (2019).
- [28] M. Zanner, T. Orell, C. M. F. Schneider, R. Albert, S. Oleschko, M. L. Juan, M. Silveri, and G. Kirchmair, Coherent control of a multi-qubit dark state in waveguide quantum electrodynamics, *Nat. Phys.* **18**, 538 (2022).
- [29] A. S. Sheremet, M. I. Petrov, I. V. Iorsh, A. V. Poshakinskiy, and A. N. Poddubny, Waveguide quantum electrodynamics: Collective radiance and photon-photon correlations, *Rev. Mod. Phys.* **95**, 015002 (2023).
- [30] A. Tiranov, V. Angelopoulou, C. J. v. Diepen, B. Schirnski, O. A. D. Sandberg, Y. Wang, L. Midolo, S. Scholz, A. D. Wieck, A. Ludwig, A. S. Sørensen, and P. Lodahl, Collective super- and subradiant dynamics between distant optical quantum emitters, *Science* **379**, 389 (2023).
- [31] G. S. Agarwal and R. R. Puri, Cooperative behavior of atoms irradiated by broadband squeezed light, *Phys. Rev. A* **41**, 3782 (1990).
- [32] B. Kraus and J. I. Cirac, Discrete entanglement distribution with squeezed light, *Phys. Rev. Lett.* **92**, 013602 (2004).
- [33] S. Zippilli, M. Paternostro, G. Adesso, and F. Illuminati, Entanglement replication in driven dissipative many-body systems, *Phys. Rev. Lett.* **110**, 040503 (2012).
- [34] K. Stannigel, P. Rabl, and P. Zoller, Driven-dissipative preparation of entangled states in cascaded quantum-optical networks, *New J. Phys.* **14**, 063014 (2012).
- [35] T. Ramos, H. Pichler, A. J. Daley, and P. Zoller, Quantum spin dimers from chiral dissipation in cold-atom chains, *Phys. Rev. Lett.* **113**, 237203 (2014).
- [36] A. L. Grimsmo and A. Blais, Squeezing and quantum state engineering with Josephson travelling wave amplifiers, *npj Quantum Inf.* **3**, 20 (2017).
- [37] J. You, Z. Liao, S.-W. Li, and M. S. Zubairy, Waveguide quantum electrodynamics in squeezed vacuum, *Phys. Rev. A* **97**, 023810 (2018).
- [38] N. Didier, J. Guillaud, S. Shankar, and M. Mirrahimi, Remote entanglement stabilization and concentration by quantum reservoir engineering, *Phys. Rev. A* **98**, 012329 (2018).
- [39] L. C. G. Govia, A. Lingenfelter, and A. A. Clerk, Stabilizing two-qubit entanglement by mimicking a squeezed environment, *Phys. Rev. Res.* **4**, 023010 (2022).
- [40] J. Agustí, Y. Minoguchi, J. M. Fink, and P. Rabl, Long-distance distribution of qubit-qubit entanglement using Gaussian-correlated photonic beams, *Phys. Rev. A* **105**, 062454 (2022).
- [41] J. Agustí, X. H. H. Zhang, Y. Minoguchi, and P. Rabl, Autonomous distribution of programmable multi-qubit entanglement in a dual-rail quantum network, *Phys. Rev. Lett.* **131**, 250801 (2023).
- [42] R. Gutiérrez-Jáuregui, A. Asenjo-Garcia, and G. S. Agarwal, Dissipative stabilization of dark quantum dimers via squeezed vacuum, *Phys. Rev. Res.* **5**, 013127 (2023).
- [43] H. Pichler, T. Ramos, A. J. Daley, and P. Zoller, Quantum optics of chiral spin networks, *Phys. Rev. A* **91**, 042116 (2015).
- [44] K. Lalumière, B. C. Sanders, A. F. van Loo, A. Fedorov, A. Wallraff, and A. Blais, Input-output theory for waveguide QED with an ensemble of inhomogeneous atoms, *Phys. Rev. A* **88**, 043806 (2013).
- [45] This condition can be relaxed at the expense of realizing chiral emission into the waveguide [34,35,41,43].
- [46] C. Eichler, D. Bozyigit, C. Lang, L. Steffen, J. Fink, and A. Wallraff, Experimental state tomography of itinerant single microwave photons, *Phys. Rev. Lett.* **106**, 220503 (2011).
- [47] C. Lang, C. Eichler, L. Steffen, J. M. Fink, M. J. Woolley, A. Blais, and A. Wallraff, Correlations, indistinguishability and entanglement in Hong-Ou-Mandel experiments at microwave frequencies, *Nat. Phys.* **9**, 345 (2013).
- [48] J. Ilves, S. Kono, Y. Sunada, S. Yamazaki, M. Kim, K. Koshino, and Y. Nakamura, On-demand generation and characterization of a microwave time-bin qubit, *npj Quantum Inf.* **6**, 34 (2020).
- [49] B. Kannan, D. L. Campbell, F. Vasconcelos, R. Winik, D. K. Kim, M. Kjaergaard, P. Krantz, A. Melville, B. M. Niedzielski, J. L. Yoder, T. P. Orlando, S. Gustavsson, and W. D. Oliver, Generating spatially entangled itinerant photons with waveguide quantum electrodynamics, *Sci. Adv.* **6**, eabb8780 (2020).
- [50] W. K. Wootters, Entanglement of formation of an arbitrary state of two qubits, *Phys. Rev. Lett.* **80**, 2245 (1998).
- [51] F. Yan, S. Gustavsson, J. Bylander, X. Jin, F. Yoshihara, D. G. Cory, Y. Nakamura, T. P. Orlando, and W. D. Oliver, Rotating-frame relaxation as a noise spectrum analyser of a superconducting qubit undergoing driven evolution, *Nat. Commun.* **4**, 1 (2013).
- [52] G. Ithier, E. Collin, P. Joyez, P. J. Meeson, D. Vion, D. Esteve, F. Chiarello, A. Shnirman, Y. Makhlin, J. Schrieffer, and G. Schön, Decoherence in a superconducting quantum bit circuit, *Phys. Rev. B* **72**, 134519 (2005).
- [53] A. Narla, S. Shankar, M. Hatridge, Z. Leghtas, K. M. Sliwa, E. Zalys-Geller, S. O. Mundhada, W. Pfaff, L. Frunzio, R. J. Schoelkopf, and M. H. Devoret, Robust concurrent remote

- entanglement between two superconducting qubits, *Phys. Rev. X* **6**, 031036 (2016).
- [54] P. Kurpiers, P. Magnard, T. Walter, B. Royer, M. Pechal, J. Heinsoo, Y. Salathé, A. Akin, S. Storz, J.-C. Besse, S. Gasparinetti, A. Blais, and A. Wallraff, Deterministic quantum state transfer and remote entanglement using microwave photons, *Nature* **558**, 264 (2018).
- [55] N. Leung, Y. Lu, S. Chakram, R. K. Naik, N. Earnest, R. Ma, K. Jacobs, A. N. Cleland, and D. I. Schuster, Deterministic bidirectional communication and remote entanglement generation between superconducting qubits, *npj Quantum Inf.* **5**, 1 (2019).
- [56] P. Campagne-Ibarcq, E. Zalys-Geller, A. Narla, S. Shankar, P. Reinhold, L. Burkhardt, C. Axline, W. Pfaff, L. Frunzio, R. J. Schoelkopf, and M. H. Devoret, Deterministic remote entanglement of superconducting circuits through microwave two-photon transitions, *Phys. Rev. Lett.* **120**, 200501 (2018).
- [57] C. J. Axline, L. D. Burkhardt, W. Pfaff, M. Zhang, K. Chou, P. Campagne-Ibarcq, P. Reinhold, L. Frunzio, S. M. Girvin, L. Jiang, M. H. Devoret, and R. J. Schoelkopf, On-demand quantum state transfer and entanglement between remote microwave cavity memories, *Nat. Phys.* **14**, 705 (2018).
- [58] Y. Zhong, H.-S. Chang, A. Bienfait, É. Dumur, M.-H. Chou, C. R. Conner, J. Grebel, R. G. Povey, H. Yan, D. I. Schuster, and A. N. Cleland, Deterministic multi-qubit entanglement in a quantum network, *Nature* **590**, 571 (2021).
- [59] J. Niu, *et al.*, Low-loss interconnects for modular superconducting quantum processors, *Nat. Electron.* **6**, 235 (2023).
- [60] I. Söllner, S. Mahmoodian, S. L. Hansen, L. Midolo, A. Javadi, G. Kiršanskė, T. Pregonato, H. El-Ella, E. H. Lee, J. D. Song, S. Stobbe, and P. Lodahl, Deterministic photon-emitter coupling in chiral photonic circuits, *Nat. Nanotechnol.* **10**, 775 (2015).
- [61] M. Scheucher, A. Hilico, E. Will, J. Volz, and A. Rauschenbeutel, Quantum optical circulator controlled by a single chirally coupled atom, *Science* **354**, 1577 (2016).
- [62] B. Kannan, A. Almanakly, Y. Sung, A. Di Paolo, D. A. Rower, J. Braumüller, A. Melville, B. M. Niedzielski, A. Karamlou, K. Serniak, A. Vepsäläinen, M. E. Schwartz, J. L. Yoder, R. Winik, J. I.-J. Wang, T. P. Orlando, S. Gustavsson, J. A. Grover, and W. D. Oliver, On-demand directional photon emission using waveguide quantum electrodynamics, *Nat. Phys.* **19**, 394 (2023).
- [63] E. S. Redchenko, A. V. Poshakinskiy, R. Sett, M. Žemlička, A. N. Poddubny, and J. M. Fink, Tunable directional photon scattering from a pair of superconducting qubits, *Nat. Commun.* **14**, 2998 (2023).
- [64] C. Joshi, F. Yang, and M. Mirhosseini, Resonance fluorescence of a chiral artificial atom, *Phys. Rev. X* **13**, 021039 (2023).
- [65] X. Cao, A. Irfan, M. Mollenhauer, K. Singirikonda, and W. Pfaff, Parametrically controlled chiral interface for superconducting quantum devices, *ArXiv:2405.15086*.
- [66] E. S. Fried, P. Sivarajah, N. Didier, E. A. Sete, M. P. da Silva, B. R. Johnson, and C. A. Ryan, Assessing the influence of broadband instrumentation noise on parametrically modulated superconducting qubits, *ArXiv:1908.11370*.
- [67] A. Irfan, M. Yao, A. Lingenfelter, X. Cao, A. A. Clerk, and W. Pfaff, Loss resilience of driven-dissipative remote entanglement in chiral waveguide quantum electrodynamics, *ArXiv:2404.00142*.
- [68] A. Lingenfelter, M. Yao, A. Pocklington, Y.-X. Wang, A. Irfan, W. Pfaff, and A. A. Clerk, Exact results for a boundary-driven double spin chain and resource-efficient remote entanglement stabilization, *Phys. Rev. X* **14**, 021028 (2024).
- [69] M. D. Hutchings, J. B. Hertzberg, Y. Liu, N. T. Bronn, G. A. Keefe, M. Brink, J. M. Chow, and B. L. T. Plourde, Tunable superconducting qubits with flux-independent coherence, *Phys. Rev. Appl.* **8**, 044003 (2017).
- [70] Z. Chen, A. Megrant, J. Kelly, R. Barends, J. Bochmann, Y. Chen, B. Chiaro, A. Dunsworth, E. Jeffrey, J. Y. Mutus, P. J. J. O'Malley, C. Neill, P. Roushan, D. Sank, A. Vainsencher, J. Wenner, T. C. White, A. N. Cleland, and J. M. Martinis, Fabrication and characterization of aluminum airbridges for superconducting microwave circuits, *Appl. Phys. Lett.* **104**, 052602 (2014).
- [71] O. Painter, S. M. M. Niri, E. J. Kim, A. Sipahigil, V. T. dos Santos Ferreira, A. J. Keller, M. Kalae, and M. T. Fang, California Institute of Technology (Caltech), Shielded bridges for quantum circuits (2020), [Online; accessed October 4, 2022], <https://patents.google.com/patent/US20210151844A1/en>.
- [72] N. Gheeraert, S. Kono, and Y. Nakamura, Programmable directional emitter and receiver of itinerant microwave photons in a waveguide, *Phys. Rev. A* **102**, 053720 (2020).
- [73] A. F. Kockum, G. Johansson, and F. Nori, Decoherence-free interaction between giant atoms in waveguide quantum electrodynamics, *Phys. Rev. Lett.* **120**, 140404 (2018).
- [74] F. Mallet, F. R. Ong, A. Palacios-Laloy, F. Nguyen, P. Bertet, D. Vion, and D. Esteve, Single-shot qubit readout in circuit quantum electrodynamics, *Nat. Phys.* **5**, 791 (2009).
- [75] B. Kannan, Ph.D. thesis, Massachusetts Institute of Technology, 2022.
- [76] C. Eichler, Ph.D. thesis, ETH Zurich, 2013.
- [77] V. T. d. S. Ferreira, Ph.D. thesis, California Institute of Technology, 2022.
- [78] To obtain the reported errors for n_{eff} , we have averaged 3×10^9 measurements over the course of 20 h.
- [79] C. Macklin, K. O'Brien, D. Hover, M. E. Schwartz, V. Bolkhovskoy, X. Zhang, W. D. Oliver, and I. Siddiqi, A near-quantum-limited Josephson traveling-wave parametric amplifier, *Science* **350**, 307 (2015).
- [80] J. Bylander, S. Gustavsson, F. Yan, F. Yoshihara, K. Harrabi, G. Fitch, D. G. Cory, Y. Nakamura, J.-S. Tsai, and W. D. Oliver, Noise spectroscopy through dynamical decoupling with a superconducting flux qubit, *Nat. Phys.* **7**, 565 (2011).
- [81] F. Yoshihara, Y. Nakamura, F. Yan, S. Gustavsson, J. Bylander, W. D. Oliver, and J.-S. Tsai, Flux qubit noise spectroscopy using Rabi oscillations under strong driving conditions, *Phys. Rev. B* **89**, 020503 (2014).
- [82] D. H. Slichter, R. Vijay, S. J. Weber, S. Boutin, M. Boissonneault, J. M. Gambetta, A. Blais, and I. Siddiqi, Measurement-induced qubit state mixing in circuit QED from up-converted dephasing noise, *Phys. Rev. Lett.* **109**, 153601 (2012).

- [83] J. Johansson, P. Nation, and F. Nori, QuTip: An open-source PYTHON framework for the dynamics of open quantum systems, *Comput. Phys. Commun.* **183**, 1760 (2012).
- [84] J. Johansson, P. Nation, and F. Nori, QuTip 2: A PYTHON framework for the dynamics of open quantum systems, *Comput. Phys. Commun.* **184**, 1234 (2013).
- [85] J. Biznárová, A. Osman, E. Rehnman, L. Chayanun, C. Križan, P. Malmberg, M. Rommel, C. Warren, P. Delsing, A. Yurgens, J. Bylander, and A. F. Roudsari, Mitigation of interfacial dielectric loss in aluminum-silicon superconducting qubits, *NPJ Quantum Inf.* **10**, 78 (2024).